

Connecting radio pulsar, magnetars and XDINSs in a unified evolutionary framework with simulation-based inference

MICHELE RONCHI ^{1,2,3} CELSA PARDO ARAUJO ^{2,3} VANESSA GRABER ⁴ NANDA REA ^{2,3} CLARA DEHMAN ⁵
DAVIDE DE GRANDIS ^{2,3} ALESSIO MARINO ^{2,3} FRANCESCO COTI ZELATI ^{2,3} JOERI VAN LEEUWEN ¹ AND
JOSÉ A. PONS ⁵

¹*ASTRON, the Netherlands Institute for Radio Astronomy, Oude Hoogeveensedijk 4, 7991 PD Dwingeloo, The Netherlands*

²*Institute of Space Sciences (CSIC-ICE), Campus UAB, Carrer de Can Magrans s/n, 08193, Barcelona, Spain*

³*Institut d'Estudis Espacials de Catalunya (IEEC), Carrer Gran Capità 2-4, 08034 Barcelona, Spain*

⁴*Department of Physics, Royal Holloway, University of London, Egham, TW20 0EX, UK*

⁵*Departament de Física, Universitat d'Alacant, Ap. Correus 99, E-03080, Alacant, Spain*

ABSTRACT

Understanding the Galactic population of isolated neutron stars within a unified framework provides key insights into their birth properties, evolutionary pathways, and the connections between different neutron star classes. In this work, we combine observational data from radio pulsars and isolated neutron stars exhibiting quiescent X-ray emission, employing a comprehensive population synthesis approach to investigate their origin and evolution. We develop a flexible population synthesis framework that models the dynamical, rotational, and magneto-thermal evolution of neutron stars, their radio and X-ray emission, and the selection effects of radio and X-ray surveys. To simulate realistic X-ray spectra, we account for magnetospheric resonant cyclotron scattering and interstellar absorption. Additionally, we model the observational bias introduced by magnetar outbursts by linking the outburst rate to magnetic stresses in the stellar crust. We employ a simulation-based inference approach called truncated sequential neural posterior estimation to reconstruct the birth properties, such as the initial magnetic field distribution and the fraction of neutron stars born with magnetar-like properties. We find that the Galactic neutron star population is best described by a two-component log-normal distribution of birth magnetic fields, with peaks at 5×10^{12} G and 10^{14} G respectively. We also infer a neutron star birth rate of 3–4 per century, of which approximately 10–50% are born as magnetars. This in turn can help quantify magnetar potential contribution to explain the rate of powerful astrophysical transient phenomena, such as fast radio bursts, super-luminous supernovae and gamma ray bursts.

Keywords: Machine learning — Neutron stars(1108) — Population synthesis — Pulsars(1306) — Radio pulsars(1353) — Simulation-based inference

1. INTRODUCTION

Neutron stars are the compact remnants left over after the core-collapse supernova of massive stars. By combining extraordinary properties such as extreme gravity, ultra-strong magnetic fields, and rapid rotation, neutron stars represent unique laboratories to study the behavior of matter and radiation in extreme environments. They have been observed emitting across the entire electromagnetic spectrum from radio to gamma-rays and

showcase diverse emission behavior, from regular periodic pulses to more sporadic highly energetic bursts of energy. Due to this variety of properties and behavior they have been classified in different classes (see, e.g., [Harding 2013](#); [Borghese & Esposito 2023](#); [Popov 2023](#)). The bulk of known neutron stars have been discovered as isolated radio pulsars with estimated dipolar magnetic fields in the range $\sim 10^{12} - 10^{13}$ G. Decades of radio pulsar surveys have produced a statistically rich sample, now comprising over four thousand objects ([Manchester et al. 2005](#)). Among other classes of isolated neutron stars there are magnetars and X-ray Dim Isolated Neutron Stars (XDINSs). Magnetars are the neutron stars

with the strongest magnetic field exceeding 10^{14} G and both their persistent and bursting emission is believed to be powered by the dissipation and instability of their magnetic field. (see Turolla et al. 2015; Kaspi & Beloborodov 2017; Esposito et al. 2021; Rea & De Grandis 2025, for a review). XDINSs, also known as the "Magnificent Seven", are a class of isolated neutron stars with faint X-ray emission, showing an almost perfect thermal spectrum with broad absorption features (see Turolla 2009, for a review). Owing to their low luminosities, they are detectable only within a few hundred parsecs, which is why the currently known sources are all nearby. If considered unrelated to one another, the existence of several neutron star classes challenges the limits of the core-collapse supernova rate in our Galaxy (Keane & Kramer 2008; Rozwadowska et al. 2021; Pardo-Araujo et al. 2026). Furthermore, in recent years the borders between the different classes of isolated neutron stars have started to blur. For example, magnetar-like burst activity has been discovered in some rotation-powered pulsars (Gavriil et al. 2008; Archibald et al. 2016) whereas pulsed radio emission was detected from several magnetars in outburst (e.g. Camilo et al. 2006). Furthermore, magnetar-like emission and faint radio emission have been detected by yet another class, central compact objects (CCOs) (Rea et al. 2016; D’Ai et al. 2016; Zhang et al. 2025), young neutron stars found at the geometrical center of supernova remnants and previously detected only as stable X-ray emitters. These observational hybrid properties indicate that the different classes of isolated neutron stars are likely connected through evolutionary pathways, and therefore should be studied as a single population rather than as distinct, unrelated categories. A unified approach helps to better understand the birth properties, the relation with their massive progenitors and supernova explosion that leads to their formation.

In general the neutron star distribution in the spin period derivative, \dot{P} , vs spin period, P , plane encodes information about the initial spin and magnetic field distributions at birth and the evolutionary pathways of the population. Population synthesis represents a powerful computational framework used to simulate the birth, evolution, and observable properties of the populations of neutron stars in the Galaxy with the aim of comparing with the observed population and constrain physical models. Due to the rich radio pulsar sample the main efforts of population synthesis studies have been focused on modelling solely the radio pulsar population (e.g. Narayan & Ostriker 1990; Faucher-Giguère & Kaspi 2006; Gullón et al. 2014; Cieřlar et al. 2020; Graber et al. 2024; Pardo-Araujo et al. 2025). However, radio pulsars

represent only a subset of the underlying neutron star population, and analyses based solely on radio detections may bias the inferred birth properties.

Both magnetars and XDINSs probe regimes of magnetic field strengths and evolutionary timescales poorly sampled by the radio pulsar population. Magnetars trace the young high-field end of the birth distribution and exhibit strong magnetic field decay, whereas XDINSs likely represent an evolved population of middle-aged, cooling neutron stars and are believed to be old magnetars (Viganò et al. 2013). Together, these thermally emitting sources offer crucial leverage on the shape and width of the initial magnetic field distribution, on the role of magnetic field decay, and on the connection between different neutron star classes. In particular understanding the birth magnetic field distribution gives important clues on the formation mechanism during supernova explosion and the fraction of neutron stars that are born as magnetars (Makarenko et al. 2021; Pardo-Araujo et al. 2026), which in turn have important implications for studying the connections with fast radio bursts (FRBs) and gamma-ray bursts (GRBs) (see, e.g. Rea et al. 2015; Stratta et al. 2018; Beniamini et al. 2025; Zhang & Hu 2025).

Recent advances in magneto-thermal evolutionary models (Viganò et al. 2021; De Grandis et al. 2021; Dehman et al. 2023c,b; Ascenzi et al. 2024) provide an improved theoretical basis for studying the evolutionary links between these classes of neutron stars and interpreting them in a unified framework. Incorporating realistic prescriptions for magnetic field decay, envelope composition, and the interplay between magnetic evolution and thermal cooling makes it possible to model not only radio pulsars but also X-ray-bright neutron stars within a single evolutionary scheme. Combining such models with population synthesis has been attempted in a few studies in the past couple of decades (e.g. Popov et al. 2010; Gullón et al. 2015). These studies showed that adding the thermally emitting neutron stars helps to break degeneracies between simulation parameters and better constrain their ranges, especially for the ones describing the initial magnetic field distribution. In particular Gullón et al. (2015) showed that a single log-normal distribution for the initial magnetic fields is unlikely to explain both populations of radio pulsars and magnetars and an extra component extending to fields up to 5×10^{14} G is required.

In this work, we use the software ML-Poppyns¹ (Ronchi et al. 2021; Graber et al. 2024; Pardo-Araujo

¹ <https://ice-csic-astroexotic.github.io/code/ml-poppyns/>

et al. 2025) to perform a comprehensive population synthesis study aimed at constraining the birth and evolutionary properties of isolated neutron stars by jointly considering the radio pulsar population and the thermally emitting neutron stars, including magnetars and XDINSs. By combining realistic magneto-thermal evolutionary tracks with emission models in the radio and X-ray bands and survey-specific selection biases, we explore whether a unified scenario with a unique set of birth properties can account for the observed diversity of neutron stars. This multi-population, multi-wavelength approach provides a more complete picture of neutron star birth properties and offers new insights into the connections between distinct observational classes.

The paper is structured in the following way: in Section 2 we describe the observed dataset of radio pulsars and X-ray emitting neutron stars used in this work; in Section 3 we explain the ingredients of the ML-Poppyns population synthesis framework; in Section 4 we highlight the simulation based inference algorithm used to perform the parameter inference; in Section 5 we describe the results and in Section 6 we discuss their implication and compare with other works.

2. OBSERVED NEUTRON STAR POPULATION

2.1. Radio pulsars

We consider the same observational sample as described in Pardo-Araujo et al. (2025) consisting of the radio pulsars detected by three major surveys conducted with Murriyang, the Parkes radio telescope: the Parkes Multibeam Pulsar Survey (PMPS) (Manchester et al. 2001; Lorimer et al. 2006), the Swinburne Intermediate-latitude Pulsar Survey (SMPS) (Edwards et al. 2001; Jacoby et al. 2009), and the low- and mid-latitude High Time Resolution Universe (HTRU) surveys (Keith et al. 2010). For the radio fluxes we consider the data from the Thousand Pulsar Array (TPA) program Johnston et al. (2020), which is part of the large survey project MeerTIME on the MeerKAT telescope. The TPA provides a consistently observed sample with well calibrated flux measurements at 1.429 GHz as reported by Posselt et al. (2023). The number of pulsars detected by these three surveys are the following:

- PMPS 1045,
- SMPS 218,
- HTRU: 1095.

The discrepancy between the number reported here for the HTRU survey and the one in the previous work of Pardo-Araujo et al. (2025) is due to reprocessing of

archival data that leads to the discovery of 58 new isolated pulsars Sengar et al. (2025). For more details on the filters applied to construct this observational dataset we refer to Pardo-Araujo et al. (2025).

2.2. Magnetars, XDINSs and other thermally emitting X-ray pulsars

The observational sample we consider includes all neutron stars that have a statistically significant thermal component in the soft X-ray band in the energy range [0.1 - 10] keV (see Table 1). The origin of this thermal emission is attributed to the residual heat stored in the neutron star interior and to the Ohmic dissipation of the magnetic field in the neutron star crust (Viganò et al. 2013, 2021). We only considered archival *Chandra* and/or *XMM-Newton* observations, as they provide the best combination of effective area and angular resolution among past and present X-rays observatories. For all sources we estimated the absorbed flux in the energy range 0.1 - 10 keV. More details on the data reduction and analysis can be found in Coti Zelati et al. (2018); Marino et al. (2024), Dehman et al., in prep.. This observational dataset we are considering contains 23 magnetars and 7 XDINSs (1 of which is missing the measurement of the spin period derivative, \dot{P}).

Magnetars have been mainly detected through episodes of very energetic outburst emissions. However, here we only consider data during their quiescence phase where their emission is mostly of thermal origin and can be described by one or more black-body components possibly with a power-law tail at higher energies that has been attributed to the resonant cyclotron scattering of the thermal seed photons emitted by the surface as they interact with the charged particles gyrating around the magnetic field lines in the magnetosphere (see Section 3.4 Rea et al. 2008; Zane et al. 2009; Beloborodov 2013).

We do not include CCOs in this work since in our simulation pipeline we are not modeling fallback accretion that could lead to the formation of objects like CCOs (Viganò & Pons 2012).

Finally, also rotation-powered pulsars (RPPs) can manifest X-ray spectra with both a thermal and a non-thermal components. Especially for the youngest ones these two components are usually attributed to the release of heat from the surface and to the synchrocurvature emission from charged particles in the magnetosphere, respectively (Becker & Truemper 1997; Xu et al. 2025). In this work, we exclude RPPs as many of them have spectra contaminated by the contribution of a pulsar-wind nebula. As the nebula is brighter in X-rays than the central neutron star, it introduces a

Table 1. Neutron stars used in this work with a significant thermal component in the quiescence phase, classified as magnetars and XDINSs. We report their spin period, P , spin-period derivative, \dot{P} , and the absorbed flux, $S_{X,\text{abs}}$, in the energy range 0.1 - 10 keV. Fluxes are reported with a 10% relative error.

Source	P [s]	\dot{P} [10^{-11} s s $^{-1}$]	$S_{X,\text{abs}}$ [erg s $^{-1}$ cm $^{-2}$]	class
SGR1627-41	2.59	1.9	4.2×10^{-14}	magnetar
1E2259+586	6.98	0.048	3.55×10^{-11}	magnetar
XTEJ1810-197	5.54	0.283	5.3×10^{-13}	magnetar
SGR1806-20	7.75	7.5	5.49×10^{-12}	magnetar
CXOUJ1647-4552	10.61	0.097	8×10^{-13}	magnetar
SGRJ0501+4516	5.76	0.594	2.5×10^{-12}	magnetar
1E1547-5408	2.07	4.77	3.2×10^{-13}	magnetar
SGRJ0418+5729	9.08	0.0004	1×10^{-14}	magnetar
SGRJ1833-0832	7.57	0.35	6×10^{-14}	magnetar
SwiftJ1822.3-1606	8.44	0.013	2.3×10^{-13}	magnetar
SwiftJ1834.9-0846	2.48	0.806	1×10^{-14}	magnetar
1E1048.1-5937	6.46	2.18	5.56×10^{-12}	magnetar
SGRJ1745-2900	3.76	3.06	2×10^{-14}	magnetar
SGRJ1935+2154	3.24	1.43	8.6×10^{-13}	magnetar
1E1841-045	11.79	4.09	2.33×10^{-11}	magnetar
SGR1900+14	5.2	9.2	3.92×10^{-12}	magnetar
4U0142+614	8.69	0.2	1.13×10^{-10}	magnetar
1RXSJ170849.0-4009	11.01	1.95	3.75×10^{-11}	magnetar
CXOUJ171405.7-3810	3.83	6.4	1.69×10^{-12}	magnetar
PSRJ1119-6127	0.407	0.4	4.8×10^{-14}	magnetar
PSRJ1622-4950	4.326	1.7	9×10^{-15}	magnetar
SwiftJ1818.0-1607	1.36	5	2.51×10^{-14}	magnetar
3XMMJ1852+0033	11.559	0.014	4.46×10^{-13}	magnetar
RXJ0420.0-5022	3.45	0.002759	5.01×10^{-13}	XDINS
RXJ1856.5-3754	7.055	0.003	2×10^{-11}	XDINS
RXJ2143.0+0654	9.428	0.0041	2.51×10^{-12}	XDINS
RXJ0720.4-3125	8.391	0.006983	1×10^{-11}	XDINS
RXJ0806.4-4123	11.37	0.0055	2.51×10^{-12}	XDINS
RXJ1308.6+2127	10.31	0.011	3.16×10^{-12}	XDINS
RXJ1605.3+3249	3.39	-	7.94×10^{-12}	XDINS

252 detection bias which we are not modelling in our simu-
 253 lations. Moreover contrary to magnetars and XDINSs,
 254 most RPPs are already detected in radio and probe a
 255 range of magnetic fields which is already well represented
 256 by the rich sample of radio pulsars.

257 3. POPULATION SYNTHESIS

258 To generate a synthetic population of neutron stars we
 259 performed Monte Carlo simulations to model both the
 260 dynamical and magneto-rotational evolution of neutron
 261 stars. We then model their radio and X-ray emission
 262 and apply observational biases both for the radio and X-
 263 ray surveys to compare the simulated populations with
 264 observations. We follow the same approach as in Ronchi
 265 et al. (2021); Graber et al. (2024); Pardo-Araujo et al.

266 (2025), hence we refer the reader to these works for more
 267 details on the employed methodology.

268 3.1. Dynamical evolution

269 Following the same approach as in Pardo-Araujo et al.
 270 (2025), we assume the dynamical properties are decou-
 271 pled from the magneto-rotational ones, therefore we cre-
 272 ate a database containing the information of a dynam-
 273 ically evolved population of neutron stars. With this
 274 purpose, we simulated a population of 2×10^7 neutron
 275 stars, assigning them uniformly distributed random ages
 276 up to 10^8 yr to ensure a sufficiently large database to
 277 sample from for the subsequent magneto-rotational evo-
 278 lution and detection.

279 For the initial positions we use the same strategy out-
 280 lined in Ronchi et al. (2021) (but see also Graber et al.

281 2024; Pardo-Araujo et al. 2025). We assume that the
 282 progenitor OB stars follow the spiral arms parametrized
 283 with a logarithmic model as in Yao et al. (2017) and the
 284 Galactocentric exponential radial distribution found by
 285 Verberne & Vink (2021) for supernova remnants. For
 286 the Galactic height we assume an exponential disk pro-
 287 file (Wainscoat et al. 1992) with a characteristic scale
 288 height of 0.18 kpc, consistent with the vertical distri-
 289 bution of young massive stars in the Milky Way (Li
 290 et al. 2019). The kick velocities are drawn from the log-
 291 normal distribution found in Disberg & Mandel (2025)
 292 with mean of 5.6 and standard deviation of 0.68. Af-
 293 ter setting the initial conditions we evolve the neutron
 294 stars positions and velocities in time by solving the New-
 295 tonian equation of motion with the same prescription
 296 as in Graber et al. (2024); Pardo-Araujo et al. (2025).
 297 In this way we obtain a dynamically evolved database
 298 of neutron stars that we can sample from to perform
 299 the following steps of the simulation, i.e., the magneto-
 300 rotational evolution and the detection.

3.2. Magneto-rotational evolution

302 In order to model the magneto-rotational evolution of
 303 neutron stars we assume that the initial spin periods
 304 follow a log-normal distribution of the form:

$$305 \quad \mathcal{P}(\log P_0) = \frac{1}{\sqrt{2\pi}\sigma_{\log P}} \exp\left(-\frac{(\log P_0 - \mu_{\log P})^2}{2\sigma_{\log P}^2}\right). \quad (1)$$

306 Here and in the following we use log to refer to \log_{10} to
 307 not clutter the notation.

308 For the initial magnetic field distribution we consider
 309 a double log-normal parametrized in the following way:

$$310 \quad \mathcal{P}(\log B_0) = w_{\log B} \mathcal{N}(\log B_0, \mu_{\log B,1}, \sigma_{\log B,1}) \\ + (1 - w_{\log B}) \mathcal{N}(\log B_0, \mu_{\log B,2}, \sigma_{\log B,2}), \quad (2)$$

311 where,

$$312 \quad \mathcal{N}(\log B_0, \mu_{\log B,i}, \sigma_{\log B,i}) = \\ \frac{1}{\sqrt{2\pi}\sigma_{\log B,i}} \exp\left(-\frac{(\log B_0 - \mu_{\log B,i})^2}{2\sigma_{\log B,i}^2}\right), \quad (3)$$

313 with $i = 1, 2$ and $w_{\log B}$ represents a weight parameter
 314 for the first component with a range between 0 and 1.

315 The choice of this model for the initial magnetic field
 316 distribution is given by the fact that a distribution ex-
 317 tended to stronger magnetic fields is required to explain
 318 the population of magnetars (see Popov et al. 2010;
 319 Gullón et al. 2015; Sautron et al. 2025). The pres-
 320 ence of two components in the initial magnetic field

321 distribution implicitly assumes that the birth magnetic
 322 field could originate either from different progenitors or
 323 mechanisms that enhance the magnetic field during the
 324 core collapse (Duncan & Thompson 1992; Barrère et al.
 325 2022).

326 The initial inclination angle χ between the spin axis
 327 and the magnetic field axis is drawn randomly from a
 328 uniform distribution in spherical coordinates, i.e., with
 329 a probability $\mathcal{P}(\chi) = \sin \chi$.

330 After establishing the initial conditions, the spin pe-
 331 riod and the inclination angle are evolved in time by
 332 solving the coupled differential equations (Spitkovsky
 333 2006; Philippov et al. 2014):

$$334 \quad \dot{P} = \frac{\pi^2 B^2 R^6}{c^3 IP} (\kappa_0 + \kappa_1 \sin^2 \chi), \quad (4)$$

$$335 \quad \dot{\chi} = -\frac{\pi^2 B^2 R^6}{c^3 IP^2} (\kappa_2 \sin \chi \cos \chi), \quad (5)$$

336 where c is the speed of light, $R = 12.59$ km is the neutron
 337 star radius for a fiducial neutron star mass $M = 1.4 M_\odot$
 338 and assuming the equation of state BSk24 (Pearson
 339 et al. 2018), and $I \simeq 2MR^2/5 \approx 1.78 \times 10^{45}$ g cm²
 340 is the stellar moment of inertia. For realistic pulsars
 341 surrounded by plasma-filled magnetospheres, we choose
 342 $\kappa_0 = \kappa_1 = \kappa_2 = 1$.

3.3. Magneto-thermal evolution models

344 To model the coupled evolution of magnetic field and
 345 thermal luminosity of neutron stars we rely on the re-
 346 sults of 2D magneto-thermal simulations (see Viganò
 347 et al. 2021). We assumed the equation of state BSk24
 348 (Pearson et al. 2018) which has been proven to be able
 349 to explain the luminosities of thermally emitting neu-
 350 tron stars (Marino et al. 2024). We assume a neutron
 351 star mass $M_{\text{NS}} = 1.4 M_\odot$ and a corresponding radius
 352 $R_{\text{NS}} = 12.59$ km. The impurity parameter in the pasta
 353 layer is fixed to 100 (Pons et al. 2013). For the impu-
 354 rity in the outer and inner crust (excluding the pasta
 355 layer), the fits of Carreau et al. (2020) have been used
 356 (see Fig. 5 in that paper). The blanketing envelope
 357 model we adopt is that of Potekhin et al. (2015), com-
 358 posed of heavy elements such as iron and accounting
 359 for magnetic-field effects. To assess the impact of dif-
 360 ferent envelope compositions and whether the envelope
 361 is magnetized on magneto-thermal evolution, we refer
 362 the reader to Dehman et al. (2023a). We consider a
 363 crust-confined magnetic field configuration that includes
 364 only the dipolar ($\ell = 1$) poloidal and toroidal magnetic
 365 field components. We set the two components to have
 366 the same magnetic strength. As a result, the poloidal
 367 dipole component contains ($\sim 90\%$) of the total mag-
 368 netic energy, while the remaining ($\sim 10\%$) is stored in

the toroidal component. In the top panel of Fig. 1 we show the poloidal dipolar magnetic field evolution with an analytical parametrization for magnetic field evolution (dashed lines). As current magnetothermal simulations can properly model the surface temperature and field evolution only until $\sim 10^6$ yrs, in this work we used the same parametrization described in Graber et al. (2024) which captures the trend of field decay for different initial magnetic field strengths by combining several broken power laws together with a late-time power-law evolution with power-law index a_{late} . Furthermore to avoid the field decaying to unrealistically small numbers at very late times, we sample the \log_{10} of the final fields from a Gaussian distribution with mean $\mu = 8.5$ and standard deviation $\sigma = 0.5$ in line with the distribution seen for old millisecond pulsars (see Appendix A in Graber et al. 2024, for more details). This allows us to easily extract the dipolar field strength, B , at different times, t , to compute the magneto-rotational evolution of our synthetic pulsars.

Together with the magnetic field decay, magneto-thermal simulations provide the coupled evolution in time of the temperature profile $T(\theta, t)$ on the neutron star surface, where θ denotes the polar angular coordinate. Given a temperature profile $T(\theta, t)$ at a given time, we can compute the total luminosity that a distant observer would estimate by assuming black body emission from every element of surface area and integrating over the neutron star surface:

$$L_{\text{th}}(t) = 2\pi \int_0^\pi \sigma_{\text{SB}} T_\infty(\theta, t)^4 R_\infty^2 \sin\theta d\theta. \quad (6)$$

Here, $\sigma_{\text{SB}} = 5.67 \times 10^{-5} \text{ erg cm}^{-2} \text{ K}^{-4} \text{ s}^{-1}$ is the Stefan-Boltzmann constant, T_∞ and R_∞ denote the temperature and neutron star radius that a distant observer would measure due to the curvature of space-time around the neutron star and are defined as:

$$T_\infty = \left(1 - \frac{2GM_{\text{NS}}}{c^2 R_{\text{NS}}}\right)^{1/2} T, \quad (7)$$

$$R_\infty = \left(1 - \frac{2GM_{\text{NS}}}{c^2 R_{\text{NS}}}\right)^{-1/2} R_{\text{NS}}. \quad (8)$$

When the temperature becomes too low the routines that model the microphysics in magneto-thermal simulations do not provide reliable results. This happens at ages between $\sim 10^5 - 10^6$ yr. To perform population synthesis simulations at late times, we need to extend the luminosity after $\sim 10^6$ yr by considering the cooling during the photon dominated era. In order to get an estimate of the thermal evolution at the late stage, we assume that the surface temperature of the envelope, T_e , is linked to the temperature at the bottom of the

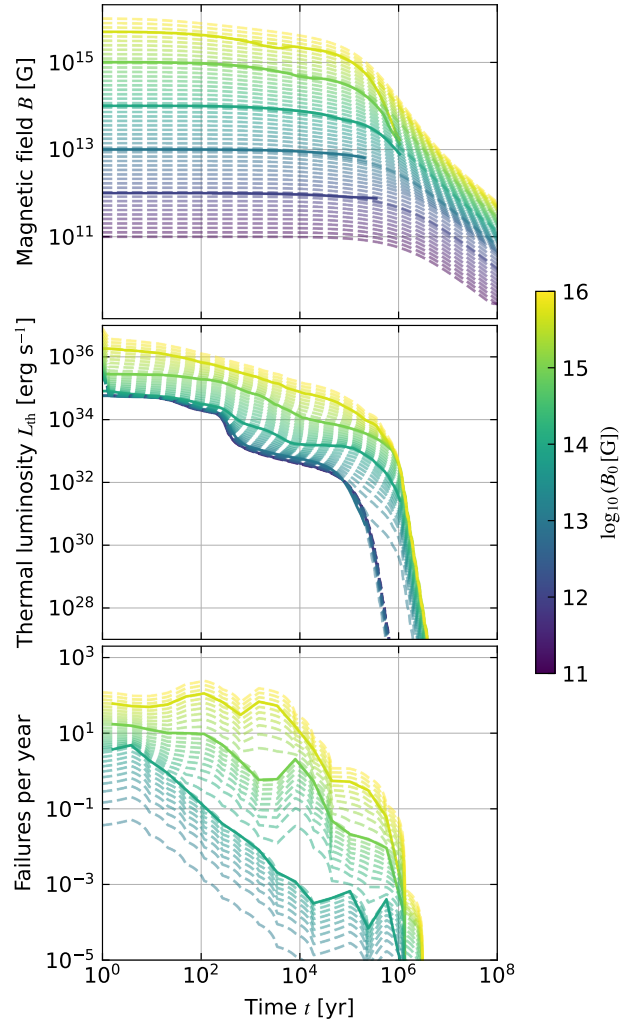


Figure 1. *Top panel:* Evolution of the poloidal dipolar B -field. The five solid curves represent realistic two-dimensional simulations of magneto-thermal evolution in the neutron-star crust (Viganò et al. 2021). The dashed lines represent the evolution predicted by the analytical prescription used in Graber et al. (2024) with the parameter $a_{\text{late}} = -1.0$. *Middle panel:* The corresponding evolution of the surface thermal luminosity. The five solid curves represent realistic two-dimensional simulations of magneto-thermal evolution in the neutron-star crust (Viganò et al. 2021). The dashed lines represent the evolution predicted by interpolating the original curve with a bivariate spline and extrapolating to a range of initial dipolar magnetic field values. *Bottom panel:* The corresponding evolution of the rate of crust failures due to magnetic stresses. The three solid curves represent the predicted crust-failure rate from realistic two-dimensional simulations of magneto-thermal evolution in the neutron-star crust (Viganò et al. 2021). The dashed lines represent the evolution predicted by interpolating the original curves with a bivariate spline and extrapolating to a range of initial dipolar magnetic field values. In all panels the colors represent the initial poloidal dipolar magnetic-field strength, B_0 .

416 envelope, T_b , at the interface with the crust via the re-
 417 lation $T_e \sim T_b^{0.5+\alpha}$, where $\alpha \sim 0.05$ (see Eq. 34 in Page
 418 et al. 2004). During the photon cooling era, we have that
 419 $T_e \propto t^{-\frac{1}{8\alpha}}$ (see Eq. 42 in Page et al. 2004) which trans-
 420 lates into a luminosity evolution $L_\gamma \propto T_e^4 \propto t^{-\frac{1}{2\alpha}} = t^{-10}$
 421 (see Eq. 38 in Page et al. 2004). Therefore for the late
 422 time evolution of the luminosity we consider a power-
 423 law with the trend $L_{\text{th}} \propto t^{-10}$. In the bottom panel of
 424 Fig. 1 we show the surface thermal luminosity evolution.
 425 As we performed simulations only for discrete values of
 426 the initial poloidal dipolar magnetic fields, in order to
 427 have an estimate of the luminosity for any initial dipol-
 428 ar magnetic field we interpolate using a bivariate spline.
 429 This approximation is used to extrapolate the luminos-
 430 ity to all initial dipolar magnetic field values in the range
 431 $10^{11} - 10^{16}$ G. These interpolated curves allow us to ob-
 432 tain the thermal luminosity of a neutron star given its
 433 initial poloidal dipolar magnetic field strength and its
 434 age.

3.4. Modelling the X-ray thermal emission

436 By having the thermal luminosity at the surface we
 437 can compute an average effective surface temperature
 438 as measured by a distant observer given by:

$$439 \quad \bar{T}_\infty = \left(\frac{L_{\text{th}}}{4\pi R_\infty^2 \sigma_{\text{SB}}} \right)^{1/4}. \quad (9)$$

440 This temperature can be used to define a black-body
 441 spectrum.

442 Magnetars spectra show a non-thermal tail that is
 443 attributed to the resonant cyclotron scattering effect
 444 (Lyutikov & Gavriil 2006; Rea et al. 2008; Nobili et al.
 445 2008). In this process the seed thermal photons coming
 446 from the neutron star surface interact with the mag-
 447 netospheric plasma composed mainly of electrons and
 448 positrons gyrating along the magnetic field lines. Pho-
 449 tons that have frequencies ω close to the cyclotron fre-
 450 quency $\omega_B = eB/(m_e c)$ will experience resonant scatter-
 451 ing and their energy will be boosted. Multiple scatter-
 452 ing events distort the observed spectrum and introduce
 453 a power-law tail at high energies.

454 To compute the intensity spectrum distorted by reso-
 455 nant cyclotron scattering, $I_{\text{RCS}}(E)$, we used the simpli-
 456 fied semi-analytical 1D model described in Lyutikov &
 457 Gavriil (2006) (see Appendix A for more details).

458 Once the scattered spectrum has been computed we
 459 can estimate the total luminosity through the integral:

$$460 \quad L_X(E) = 4\pi R_\infty^2 \int_0^{2\pi} \int_0^{\pi/2} I_{\text{RCS}}(E) \cos \theta' \sin \theta' d\theta' d\phi' \\ 461 \quad = 4\pi R_\infty^2 \pi I_{\text{RCS}}(E). \quad (10)$$

462 where θ' denotes the angle between the normal to the
 463 neutron star surface and a random line of sight direction
 464 and ϕ' is an azimuthal angle. By knowing the distance
 465 d from the neutron star we can derive the intrinsic flux
 466 density as:

$$467 \quad S_X(E) = \frac{L_X(E)}{4\pi d^2} = \pi \left(\frac{R_\infty}{d} \right)^2 I_{\text{RCS}}(E). \quad (11)$$

468 In order to compute the X-ray flux reaching the Earth
 469 we need to correct for the interstellar absorption due to
 470 photoionization. Given an intrinsic (not absorbed) X-
 471 ray flux density $S_X(E)$ where E denotes the energy in
 472 keV, the absorbed flux can be derived by (see Wilms
 473 et al. 2000):

$$474 \quad S_{X,\text{obs}}(E) = e^{-\sigma_{\text{ISM}}(E)N_{\text{H}}} S_X(E). \quad (12)$$

475 Here, $\sigma_{\text{ISM}}(E)$ in units of cm^2 per hydrogen atom rep-
 476 resents the energy-dependent effective absorption cross
 477 section of the interstellar medium (ISM) which is nor-
 478 malized on the hydrogen atom number. Taking into
 479 account the phases of the ISM this cross section can be
 480 written as:

$$481 \quad \sigma_{\text{ISM}}(E) = \sigma_{\text{gas}}(E) + \sigma_{\text{molecules}}(E) + \sigma_{\text{grains}}(E). \quad (13)$$

482 To compute $\sigma_{\text{ISM}}(E)$ we will only take into account
 483 the neutral atomic gas, that is the $\sigma_{\text{gas}}(E)$ term, ne-
 484 glecting the possibility of ionization and the presence of
 485 molecules and grains in the ISM. As shown in Wilms
 486 et al. (2000) (see also Willingale et al. 2013), including
 487 these effects would give only a minor correction to the
 488 total effective cross sections. Therefore we can rewrite
 489 the equation above as (see Wilms et al. 2000):

$$490 \quad \sigma_{\text{ISM}}(E) \sim \sigma_{\text{gas}}(E) \sim \sum_Z A_Z \sigma_{\text{ph},Z}(E), \quad (14)$$

491 where, for an element with atomic number Z , the
 492 relative abundance with respect to hydrogen is de-
 493 fined as $A_Z = N_Z/N_{\text{H}}$. Table 2 in Wilms et al.
 494 (2000) reports the logarithm of the relative abundance
 495 $\log_{10}(N_Z/N_{\text{H}}) + 12$ where by definition the abundance
 496 of hydrogen is set to 12. $\sigma_{\text{ph},Z}(E)$ denotes the photoion-
 497 ization cross section. To derive the total effective cross
 498 section $\sigma_{\text{ISM}}(E)$ we translated into Python the Fortran
 499 77 routines written by Balucinska-Church & McCam-
 500 mon (1992). The original routines implement polyno-
 501 mial fits of the atomic photoionization cross sections in
 502 the energy range of 0.03 – 10 keV for seventeen elements.

503 In Eq. (12), N_{H} denotes the hydrogen column density
 504 and has units of hydrogen atoms cm^{-2} and is defined as
 505 the integral of the spatial density of neutral hydrogen,
 506 n_{H} , along the line of sight:

$$N_{\text{H}} = \int n_{\text{H}} dl, \quad (15)$$

where l represents the path length along the line of sight. For a given neutron star with known equatorial sky coordinates (RA, DEC) and heliocentric distance d the value of N_{H} can be estimated using the reddening map of the Galaxy and the calibration factor provided by Doroshenko (2024).

The calibration factor converts reddening $E(B - V)$ provided by the map into an N_{H} value assuming a set of abundances for the ISM. By default we use the abundances specified in Wilms et al. (2000).

Finally to compute the total flux we integrate the flux density in Eq. (12) in the energy band 0.1 – 10 keV.

3.5. Crustal failures and outburst activity

Magnetars have been primarily discovered through their flaring and bursting activity, often accompanied by sudden increases with respect to their persistent thermal and non-thermal emission by several orders of magnitude that could last for months or years, a phenomenon commonly referred to as an outburst (Rea & Esposito 2011; Coti Zelati et al. 2018). This highly variable and powerful activity is supposed to be linked to reconnection events in neutron stars magnetosphere, possibly triggered by the star’s interior evolution. In particular, current models suggest that the evolution and the instability of magnetar ultra-strong magnetic field could cause mechanical stresses in the neutron star crust that could accumulate to the point of exceeding the yield of the crust, generating an event that can heat the crust up locally and drag field lines, that could ultimately propagate and trigger magnetospheric activity (Beloborodov 2009; Chugunov & Horowitz 2010; Carrasco et al. 2019; Dehman et al. 2020; Lander 2023). As the flaring and outburst activity represents a relevant bias towards the discovery of highly magnetized neutron stars, we need to model the rate of these events for a given neutron star. In this regard 2D magneto-thermal simulations provide an estimate of when and in which location the crust will fail due to the stresses mentioned above (Perna & Pons 2011; Dehman et al. 2020). This information can be used to compute the rate of crustal failures as a function of time and initial poloidal dipolar magnetic field during the magnetic field evolution. To evaluate the rate we divide the total evolution time span in logarithmic bins and count how many failure events are produced in each bin. To obtain the rate of failures in each bin we then divided the total count in each bin by the bin width.

In the bottom panel of Fig. 1 we show the rate of crust failures as a function of time predicted by the 2D simulations of magneto-thermal evolution. As we performed simulations only for discrete values of the initial

dipolar magnetic fields, in order to have an estimate of the failure rate for any initial dipolar magnetic field we interpolate using a bivariate spline. This approximation is used to extrapolate the rate to all initial dipolar magnetic field values in the range $10^{11} - 10^{16}$ G. As for the thermal luminosity, these interpolated curves allow us to obtain the crust-failure rate of a neutron star given its initial poloidal dipolar magnetic field strength and its age.

3.6. Radio detection

To compute the radio fluxes, beam geometry and propagation effects due to the interaction of the radio waves with the interstellar medium we use the same prescription as in (Graber et al. 2024; Pardo-Araujo et al. 2025). In particular, to model the intrinsic radio luminosity we adopted Eq. (7) in Pardo-Araujo et al. (2025) where the mean of the logarithm of the radio luminosity, $\mu_{\log L_0}$, and the power-law index, α_L , determining the dependence on the spin-down power, are free parameters. As in Graber et al. (2024); Pardo-Araujo et al. (2025) we consider three major radio surveys conducted with Murriyang, the Parkes radio telescope: the Parkes Multibeam Pulsar Survey (PMPS) (Manchester et al. 2001; Lorimer et al. 2006), the Swinburne Intermediate-latitude Pulsar Survey (SMPS) (Edwards et al. 2001; Jacoby et al. 2009), and the low- and mid-latitude High Time Resolution Universe (HTRU) surveys (Keith et al. 2010). A summary of all relevant survey parameters is provided in Table 1 in Graber et al. (2024). For each simulated neutron star whose radio beam intercepts our line of sight we compute the signal to noise ratio using the radiometer equation (Lorimer & Kramer 2012):

$$S/N = \varepsilon \frac{S_{\text{mean}} G \sqrt{n_{\text{pol}} \Delta f_{\text{bw}} t_{\text{obs}}}}{\beta [T_{\text{sys}} + T_{\text{sky}}(l, b)]} \sqrt{\frac{P - w_{\text{obs}}}{w_{\text{obs}}}}. \quad (16)$$

For a more detailed description of all relevant parameters in this equation we refer to Graber et al. (2024); Pardo-Araujo et al. (2025). We only stress here that compared with Graber et al. (2024); Pardo-Araujo et al. (2025), we updated the radiometer equation by including the efficiency factor, ε , a function of the duty cycle $\delta = w_{\text{obs}}/P$, determined by Morello et al. (2020) (see their Eq. 44). Since pulsars are predominantly found via incoherent searches based on Fast Fourier Transforms (FFT), this efficiency factor models the decay in sensitivity of pulsar searches when looking for pulsars with small duty cycles. Sometimes this efficiency factor is incorporated into the degradation factor β by considering values larger than ~ 1.25 . Here we fix $\beta \sim 1.25$ that only accounts for imperfections during the digitization of the signal.

3.7. Modeling the X-ray detection biases

The observational sample for the X-ray emitting neutron stars is difficult to reproduce in a simulation framework as it is subject to complex observational biases which are not well under control. Many of these sources have been discovered through targeted observations with different X-ray instruments, therefore the sky coverage and the threshold sensitivities are very inhomogeneous and difficult to reproduce in a simulation framework. Indeed many magnetars have been discovered through their outburst activity whose high energy emission triggered all-sky X-ray monitors onboard Swift–BAT or Fermi–GBM. This allowed to perform follow-up campaign observations that allowed to detect a periodicity and identify them as neutron stars Rea & Esposito (2011); Coti Zelati et al. (2018). Moreover in the observed catalog, for sources that underwent a magnetar-like outburst, we are only considering sources with a detected quiescent emission (note that some magnetars were identified as such during an outburst event but their quiescent emission is too faint to be detectable). On the other hand sources like XDINSs have very stable X-ray emission since several decades, and despite their relatively faint X-ray luminosities could be detected due to their high-fluxes, consequence of their close-by distances. To try to encompass all these different observational biases we adopt a simplified approach to model the X-ray detection.

First, we consider an all-sky coverage for X-ray surveys, i.e., we assume that X-ray instruments have scanned the entire sky. We assumed that for 0.1 – 10 keV fluxes above a value of $\sim 10^{-11} \text{ erg s}^{-1} \text{ cm}^{-2}$ the observed sample is complete. Indeed the observed $\log N - \log S$ (see black line in Fig. 4) has a change in slope at fluxes lower than $10^{-12} \text{ erg s}^{-1} \text{ cm}^{-2}$ meaning that we are probably starting missing sources at these flux values. Therefore we consider an average flux threshold of $10^{-12} \text{ erg s}^{-1} \text{ cm}^{-2}$ in the X-ray band 0.1 – 10 keV with a standard deviation (in log) of 0.5. This is also in agreement with averages flux thresholds of early all sky surveys like with ROSAT (Truemper 1982; Voges et al. 1999). This allows the detection of all sources that are intrinsically very bright or close-by like the XDINSs.

On top of this first filter, we assume a second filter for all simulated magnetar-like sources that show outburst activity. In particular, for every simulated neutron star we estimate the current crust-failure rate given its initial magnetic field and age as explained in Section 3.5. Given this rate we estimated the probability for each star to experience a crust failure event that could trigger an outburst in the last 30 years. Indeed continuous all-

sky monitoring capable of detecting new activity from magnetars has only been available for approximately the past 30 years, beginning with the launch of the Rossi X-ray Timing Explorer (RXTE) mission (Bradt et al. 1993). Prior to this, transient activity was significantly harder to detect, although some events may have been captured by earlier all-sky surveys such as the ROSAT. We assume that all outburst events are energetic enough to trigger a detection and a deep follow-up observations with X-ray instruments. In this case we assume an average flux threshold of $10^{-14} \text{ erg s}^{-1} \text{ cm}^{-2}$ with a standard deviation in log of 0.5. We assume this flux threshold in order to match the faintest detected magnetar (see 1). The choice for the flux threshold values considered here comes from both trying to reproduce the observed X-ray flux distribution and the typical sensitivity of X-ray instruments for low and large exposure times (see for example Fig. 3 in Watson et al. 2001; Weisskopf et al. 2002; Gehrels et al. 2004).

3.8. Representation of simulated output

The output of the simulations, consisting of the mock detected neutron stars in radio and X-rays is represented in the form of 2D $P - \dot{P}$ maps following the same strategy as in Graber et al. (2024); Pardo-Araujo et al. (2025). In particular, for each simulated survey we produce two maps: a density $P - \dot{P}$ map and an average flux map of the $P - \dot{P}$ diagram. Both types of maps have ranges set to $[0.01, 100] \text{ s}$ and $[10^{-20}, 10^{-9}] \text{ s s}^{-1}$ for the P and \dot{P} axis respectively and a resolution of 32 bins on both axis. The density map contains the information of the number of pulsars detected in each bin while the flux maps store the average value of the radio flux in Jy or the X-ray flux in $\text{erg s}^{-1} \text{ cm}^{-2}$ of the neutron stars falling in that specific bin for the radio surveys or X-ray survey respectively. Therefore the output of each simulation is summarized in a total of eight 2D maps, six for the radio surveys and two for the X-ray survey.

In Fig. 2 we show the maps for the real observed population. Note that for the X-ray population (last maps on the right) the top and bottom blobs represent the young magnetar population (with estimated age less than 2 kyr, see Section 5 for more details) and the XDINS population respectively.

In order to smooth out abrupt features in the map due to the random nature of the simulation we apply a gaussian smoothing kernel. These maps associated with the respective ground truth labels, i.e., the parameter set used to simulate them, will be the input provided to train the simulation based inference framework explained in Section 4. Furthermore, to make the training procedure more stable we standardize both maps and

710 labels so that the values have a mean of 0 and a stan-
 711 dard deviation of 1. Standardization is performed on a
 712 sample basis for the maps and on a dataset basis for the
 713 labels (see [Graber et al. 2024](#); [Pardo-Araujo et al. 2025](#),
 714 for more details).

715 4. SIMULATION-BASED INFERENCE

716 In recent years the development of machine learning
 717 has allowed the emergence of new tools to perform pa-
 718 rameter inference. Simulation based inference (SBI) is a
 719 recently developed framework that combines the power
 720 of bayesian statistics and deep learning to optimize and
 721 perform parameter inference when using complex model
 722 simulators (see [Cranmer et al. 2020](#); [Zammit-Mangion](#)
 723 [et al. 2025](#), for reviews). In this work we use a simulation
 724 based inference approach called neural posterior estima-
 725 tion (NPE) (e.g. [Papamakarios & Murray 2016](#); [Lueck-](#)
 726 [mann et al. 2017](#); [Greenberg et al. 2019](#); [Mishra-Sharma](#)
 727 [& Cranmer 2022](#); [Vasist et al. 2023](#); [Dax et al. 2021](#);
 728 [Barret & Dupourqué 2024](#)), which has been adopted
 729 to infer neutron star population parameters in recent
 730 population synthesis studies ([Graber et al. 2024](#); [Pardo-](#)
 731 [Araujo et al. 2025](#); [Sautron et al. 2025](#)). We refer the
 732 reader to these works for a more complete overview and
 733 description of the different SBI methods and of NPE in
 734 particular. In NPE a neural density estimator is trained
 735 to directly map a simulation output, \mathbf{x} , to the posterior
 736 distribution $\mathcal{P}(\boldsymbol{\theta}|\mathbf{x})$, which gives the probability for a set
 737 of model parameters, $\boldsymbol{\theta}$, to have generated the output \mathbf{x}
 738 through a stochastic simulator. The neural density esti-
 739 mator, q , is parametrised by a neural network F with
 740 weights ϕ (i.e., $q_{F(\mathbf{x},\phi)}$). The network is optimised by
 741 minimising the following loss function

$$742 \quad \mathcal{L}(\phi) = - \sum_{i=1}^N \ln q_{F(\mathbf{x}_i,\phi)}(\boldsymbol{\theta}_i) \quad (17)$$

743 over a training data set $\{\boldsymbol{\theta}_i, \mathbf{x}_i\}$ of size N . This loss is
 744 minimised when the neural density estimator approxi-
 745 mates the true posterior, that is:

$$746 \quad q_{F(\mathbf{x},\phi)}(\boldsymbol{\theta}) \approx \mathcal{P}(\boldsymbol{\theta}|\mathbf{x}). \quad (18)$$

747 In this work we adopt the sequential version of NPE
 748 called truncated sequential neural posterior estimation
 749 (TSNPE) ([Deistler et al. 2022](#); [Pardo-Araujo et al.](#)
 750 [2025](#)). The workflow of this algorithm can be summa-
 751 rized with the following steps ([Pardo-Araujo et al. 2025](#)):

- 752 1. Sample the proposal prior distribution to obtain
 753 $\boldsymbol{\theta}_i \sim \mathcal{P}(\boldsymbol{\theta})$ for $i = 1, \dots, N$ where N is the number
 754 of simulations we want to use for training.
- 755 2. Using the simulator, generate synthetic data $\mathbf{x}_i \sim$
 756 $\mathcal{P}(\mathbf{x}|\boldsymbol{\theta}_i)$ based on $\boldsymbol{\theta}_i$ from step 1.

757 3. Train the neural density estimator on the dataset
 758 composed of pairs $(\boldsymbol{\theta}_i, \mathbf{x}_i)_i$ obtained in the previous
 759 steps.

760 4. Use the trained neural density estimator to ap-
 761 proximate the posterior distribution $\mathcal{P}(\boldsymbol{\theta}|\mathbf{x}_0)$ at
 762 the observed data, \mathbf{x}_0 .

763 5. Restrict the prior distribution to the approximated
 764 posterior distribution computed in step 4 (see Sec-
 765 tion 3.3 in [Pardo-Araujo et al. 2025](#), and reference
 766 therein).

767 6. Update the proposal prior distribution with the
 768 new restricted prior and return to step 1.

769 Steps 1 to 5 are performed several times and each it-
 770 eration is commonly referred to as *training round*. In
 771 this way the posterior is iteratively refined focusing the
 772 computational resources on the region of the parameter
 773 space that is more compatible with the observed data.
 774 In each round the new generated simulations are added
 775 to the ones used in the previous rounds and used all
 776 together as a training dataset.

777 4.1. Neural posterior estimation setup

778 In this work we use the same setup as in [Graber et al.](#)
 779 [\(2024\)](#); [Pardo-Araujo et al. \(2025\)](#), we summarize here
 780 the main aspects important for this study. To setup
 781 the inference procedure and the neural density estima-
 782 tor we use the library `sbi` (v=0.22.0, [Tejero-Cantero](#)
 783 [et al. 2020](#)). The output of the simulations is repre-
 784 sented in the form of eight 2D maps as described in
 785 Section 3.8 and is processed by a convolutional neural
 786 network (CNN) as an eight-channel input. The CNN ar-
 787 chitecture is constituted by two 2D-convolutional layers,
 788 each followed by a 2D max pooling layer and a ReLU ac-
 789 tivation function ([Glorot & Bengio 2010](#)) and extracts
 790 key features into a latent vector of size 32. This la-
 791 tent vector is the input to the neural density estima-
 792 tor which is a mixture density network (MDN) with
 793 three fully connected layers with 32 neurons each and
 794 ReLU activation function, followed by an output layer
 795 comprising four fully connected sub-layers, correspond-
 796 ing to the mean, weight, diagonal, and upper triangular
 797 components of the covariance matrices for the Gaussian
 798 mixture (see Fig. 6 in [Graber et al. 2024](#)). We use 10
 799 Gaussian components in the mixture to ensure sufficient
 800 flexibility when approximating the posterior. We fix the
 801 batch size to 8, the fraction of training dataset to use for
 802 validation to 0.1 and train both the CNN and the MDN
 803 simultaneously using the Adam optimiser ([Kingma &](#)
 804 [Ba 2014](#)) with an initial learning rate of 5×10^{-4} and an
 805 early stopping criterion of 20 epochs to prevent overfit-

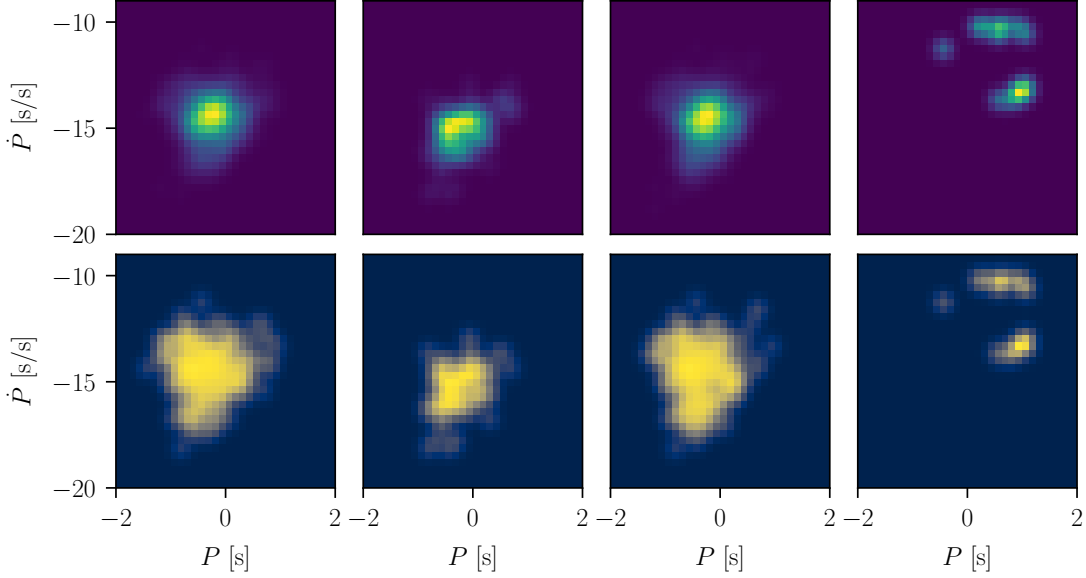


Figure 2. The eight density maps for the observed population of neutron stars. The top and the bottom row show the P - \dot{P} diagrams and the P - \dot{P} averaged flux maps for the PMPS, SMPS, HTRU, and X-ray surveys, respectively. In the top row, the color represents the density in neutron star number within each bin, while in the bottom row the color represents the averaged flux in Jy for the radio survey maps and in $\text{erg s}^{-1} \text{cm}^{-2}$ for the X-ray survey map within each bin. For bins without any stars in the bottom row, the averaged flux in log scale has been set to -7 and -17 for the radio and X-ray maps respectively.

806 ting. This implies that training is stopped if the valida-
 807 tion metric (given by the same Eq. 17 computed over the
 808 validation dataset) does not improve for 20 consecutive
 809 epochs, with the best validation weights saved. At each
 810 training round the weights for the CNN are re-initialized
 811 using the Kaiming prescription (He et al. 2015), while
 812 for the MDN the weights are initialised with PyTorch’s
 813 default initialisation. Moreover in order to take into ac-
 814 count the variance of the initialization and the training
 815 process in each round we train an ensemble of 5 neu-
 816 ral networks with identical architectures as described
 817 above. The final posterior in each round is then given
 818 by a weighted sum with equal weights of the individual
 819 posterior distributions computed by each network (see
 820 Graber et al. 2024; Pardo-Araujo et al. 2025, for more
 821 details). In each of the experiments described below in
 822 Sections 5.1 and 5.2 we train the TSNPE algorithm over
 823 10 rounds. In the first round we use 30000 simulations
 824 for training and validation and 3000 for testing purposes.
 825 In the first round we adopt the following uniform prior
 826 ranges for the parameters:

$$\begin{aligned}
 827 \quad & \mu_{\log P} \in \mathcal{U}(-1.5, 0.5), \\
 828 \quad & \sigma_{\log P} \in \mathcal{U}(0.1, 1), \\
 829 \quad & \mu_{\log B,1} \in \mathcal{U}(12, 13.5), \\
 830 \quad & \sigma_{\log B,1} \in \mathcal{U}(0.1, 1), \\
 831 \quad & \mu_{\log B,2} \in \mathcal{U}(13.5, 15), \\
 832 \quad & \sigma_{\log B,2} \in \mathcal{U}(0.1, 1),
 \end{aligned} \tag{19}$$

$$\begin{aligned}
 833 \quad & w_{\log B} \in \mathcal{U}(0.1, 1), \\
 834 \quad & a_{\text{late}} \in \mathcal{U}(-3, -0.5), \\
 835 \quad & \mu_{\log L_0} \in \mathcal{U}(24.6, 28.6), \\
 836 \quad & \alpha_L \in \mathcal{U}(0.1, 1).
 \end{aligned}$$

837 In each of the following rounds we generate 1000 new
 838 simulations by sampling the restricted prior. This num-
 839 ber has been chosen arbitrarily but as in Pardo-Araujo
 840 et al. (2025) it guarantees a good compromise between
 841 computational costs and network convergence as shown
 842 in Fig. 5. We then retrain the ensemble on the new
 843 dataset formed by adding the new simulations to the
 844 ones of the previous round. The training process is
 845 executed on a Tesla V100 SXM2 GPU with 32 GB of
 846 memory. The generation of simulations in each TSNPE
 847 round for both the training and test datasets are paral-
 848 lelled to speed up the algorithm. For this, we use the
 849 Python package Dask (Dask Development Team 2016),
 850 a library for dynamic task scheduling. In total, 600 CPU
 851 workers are employed to handle the parallelised simula-
 852 tions.

853 5. RESULTS

854 5.1. Inference on the entire population

855 We first train the TSNPE algorithm over 10 rounds
 856 with the setup explained in Section 4.1 considering the
 857 entire observed population of radio and X-ray emitting
 858 neutron stars described in Section 2.

Table 2. Comparison between best parameters values inferred by considering the whole sample of radio pulsars and X-ray emitting neutron stars (Radio + X-ray) and by considering the radio pulsars and a restricted sample with only the young magnetars and the XDINSs (Radio + young mag, XDINSs).

Parameter	Radio + X-ray	Radio + young mag, XDINSs
$\mu_{\log P}$	$-0.19^{+0.45}_{-0.73}$	$-0.26^{+0.44}_{-0.46}$
$\sigma_{\log P}$	$0.61^{+0.28}_{-0.33}$	$0.70^{+0.23}_{-0.34}$
$\mu_{\log B,1}$	$12.70^{+0.26}_{-0.23}$	$12.72^{+0.20}_{-0.21}$
$\sigma_{\log B,1}$	$0.45^{+0.11}_{-0.12}$	$0.45^{+0.13}_{-0.13}$
$\mu_{\log B,2}$	$13.85^{+0.41}_{-0.32}$	$14.11^{+0.53}_{-0.51}$
$\sigma_{\log B,2}$	$0.35^{+0.18}_{-0.19}$	$0.49^{+0.35}_{-0.32}$
$w_{\log B}$	$0.83^{+0.16}_{-0.22}$	$0.74^{+0.21}_{-0.25}$
a_{late}	$-0.89^{+0.31}_{-0.32}$	$-0.85^{+0.26}_{-0.26}$
$\mu_{\log L_0}$	$25.78^{+0.24}_{-0.24}$	$25.70^{+0.25}_{-0.26}$
α_L	$0.71^{+0.09}_{-0.09}$	$0.73^{+0.09}_{-0.09}$

After round 5 the approximated posterior results are stable therefore we use the model trained in this round to infer the best parameter values. In the first column of the table 2 we list the median of the best inferred parameters from round 5 with the 95% credible interval.

We sample 100 parameter sets from this posterior distribution and generate the respective simulations. In this way we take into account the uncertainty on the inferred parameters and their correlation. We then compare the results of these simulated populations with the real observed populations. In Fig. 3 we show the comparison between our best simulations and the observed dataset in the $P - \dot{P}$ diagram. The contour lines represent the number density of the simulated populations plotted over the real observed radio pulsars (dots) and X-ray emitting neutron stars (crosses). Both the radio pulsar population as well the entire X-ray emitting neutron star populations are well reproduced by the simulations.

However if we focus our attention on the sub-populations of young magnetars (pink crosses and contour lines) and of the XDINSs (orange crosses and contour lines), our simulations struggle to reproduce the observations. To define the sub-population of young magnetars we follow Pardo-Araujo et al. (2026) and select from the observed dataset the ones whose age estimated from a supernova remnant association or from the characteristic age is lower than 2 kyr (pink crosses). To compare with this sub-sample in our simulations we then select the neutron stars with simulated ages lower than 2 kyr (pink contour lines). For the sub-population of XDINS-like sources (orange contour lines) we consider

the simulated neutron stars within a distance of ~ 500 pc from the Sun and an age greater than 10^5 yr to mimic the properties of the observed XDINSs. While the simulations are able to predict a number of detected young magnetars of 6 ± 3 , which is compatible with the seven observed, they predict their distribution to be shifted at lower spin periods and spin-period derivatives. On the other hand, for the XDINSs the simulations are able to reproduce their timing properties but they underestimate their number to be 2 ± 2 compared to the seven observed sources.

By counting the number of neutron stars we need to generate in each simulation to reach the observed detected numbers in each survey (see Section 2) we can estimate a neutron star birth rate for each of the simulated survey. The estimated mean and standard deviation of the birth rates for the different surveys are the following:

$$\begin{aligned}
 \text{PMPS: } & \sim 3.6 \pm 0.8 \text{ neutron stars per century,} \\
 \text{SMPS: } & \sim 3.0 \pm 0.7 \text{ neutron stars per century,} \\
 \text{HTRU: } & \sim 3.0 \pm 0.7 \text{ neutron stars per century,} \\
 \text{X-ray: } & \sim 3.1 \pm 0.9 \text{ neutron stars per century,}
 \end{aligned}
 \tag{20}$$

Note that these values are compatible between each other at $1\text{-}\sigma$ level but are higher than the core collapse supernovae rate of 1.63 ± 0.46 per century estimated by Rozwadowska et al. (2021).

In Fig. 4 we compare the observed $\log N - \log S$ distribution for the absorbed X-ray fluxes (black line) with the one predicted by the simulations (purple line and bands). The observed $\log N - \log S$ is marginally consistent falling inside the $3\text{-}\sigma$ uncertainty of the simulations. However, in our simulations we observe a lack of bright sources with fluxes above $\sim 10^{-12} \text{ erg s}^{-1} \text{ cm}^{-2}$. Since the tail at high fluxes is where young or nearby bright sources dominate and where the completeness level of the observed sample is higher, this lack of sources in our model is another indication that the simulations either underestimate the detected numbers or the observed fluxes for these two sub-populations (see Section 6 for more discussion about this aspect).

5.2. Inference on the sub-sample of young X-ray population and XDINSs

As a second experiment we check the impact on our inference results of considering only the restricted samples of young magnetars and XDINSs as defined in the previous section. This should represent a less biased and more complete sample. Young sources are intrinsically rare and X-ray bright, therefore, observational biases are not expected to significantly affect their detection.

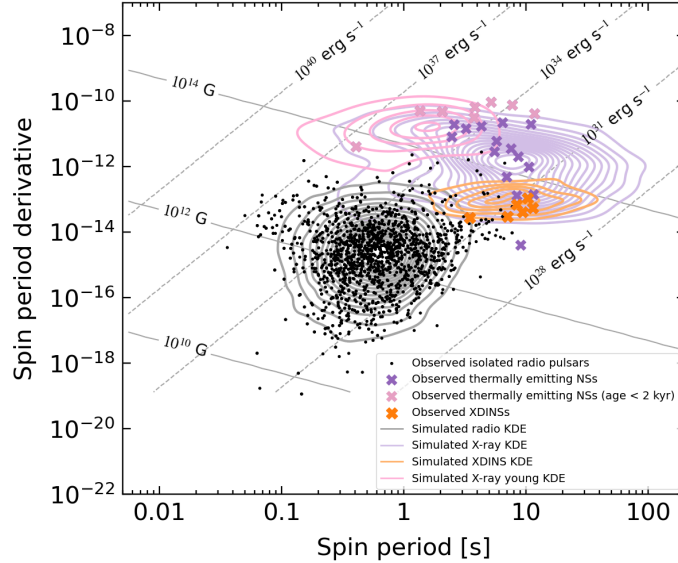


Figure 3. Comparison in the $P - \dot{P}$ diagram between the observed population of radio pulsars and X-ray emitting neutron stars and the best simulated populations assuming a double log-normal initial magnetic field distribution. Points and crosses represent the observed radio pulsars and X-ray emitting neutron stars. Pink crosses represents the young (estimated ages lower than 2 kyrs) magnetars, while orange crosses the observed XDINSSs. The contour lines represent density contours obtained from 100 simulations generated from sets of input parameters drawn from the posterior distribution obtained from round 5.

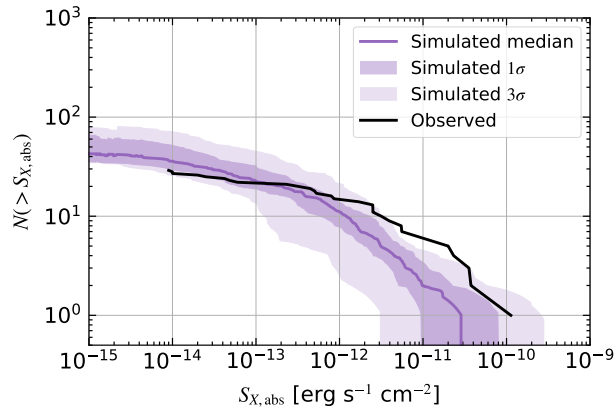


Figure 4. Comparison of the $\log N - \log S$ distributions for the observed and simulated X-ray thermally emitting neutron stars. The black line represents the trend for the observed population while the purple line and bands represent the median, the 1σ and 3σ uncertainties computed over 100 simulations generated from sets of parameters drawn from the posterior distribution obtained from round 5.

940 XDINSSs on the other hand are observed to have a high
 941 X-ray flux due to their proximity. These should repre-
 942 sent an almost complete sample considering a limiting
 943 distance of ~ 500 pc from the Sun (in Kurpas et al.
 944 2026, they discuss possible new candidates, with only
 945 one being closer than 500 pc). This results in a total
 946 of 13 X-ray bright sources to use for inference beside
 947 the radio pulsar population. We generate the maps us-
 948 ing this extra filter on the X-ray population for both
 949 the simulations and the observed sample and train the
 950 TSNPE algorithm. The inferred posterior distribution
 951 conditioned on these restricted observed data for each

952 round are displayed in Fig. 5. As in the previous experi-
 953 ment, overall the posterior distribution is stable over the
 954 training rounds.

955 In order to compare the simulated population from the
 956 best parameters inferred from the posterior with the real
 957 one, we choose to use the posterior estimate from round
 958 5 as it displays conservative results which encompass
 959 the ranges of the posterior estimated in the following
 960 rounds. To assess the quality of the trained posterior
 961 estimator in this round we check its predictive power
 962 over the test dataset by comparing its posterior predic-
 963 tions compared to the ground truth labels (see Fig. 11).

Moreover we computed the coverage probability over the same test dataset (see Fig. 12) which shows that the approximated posteriors are conservative since the coverage probability is overall greater than the credibility level (Hermans et al. 2021; Graber et al. 2024; Pardo-Araujo et al. 2025, see Appendix B for more details). These aspects highlight the robustness of the inference results. In the second column of table 2 we list the median of the best inferred parameters from round 5 with the 95% credible interval.

As in the previous section we sample 100 parameter sets from this posterior distribution and generate the respective simulations. We then compare the distributions of these simulated populations with the real observed populations in the $P - \dot{P}$ diagram (see Fig. 7). The radio pulsar population is still well reproduced by the simulations. On the other hand, when looking at the X-ray population, while this time the young magnetars (pink crosses) and XDINSs (orange crosses) are well reproduced by the simulations, the bulk of the mock observed X-ray emitting neutron stars (purple contour lines) is shifted towards longer periods when compared with the real data.

The estimated mean and standard deviation of the birth rates for the different surveys are the following:

$$\begin{aligned} \text{PMPS: } & \sim 3.8 \pm 0.8 \text{ neutron stars per century,} \\ \text{SMPS: } & \sim 3.2 \pm 0.7 \text{ neutron stars per century,} \\ \text{HTRU: } & \sim 3.2 \pm 0.7 \text{ neutron stars per century,} \\ \text{X-ray: } & \sim 0.9 \pm 0.5 \text{ neutron stars per century,} \end{aligned} \quad (21)$$

Note that also in this case the predicted core collapse supernovae rate is larger than the value from Rozwadowska et al. (2021). In particular while the values of the three radio surveys are still compatible between each other at 1- σ level, for the X-ray survey the mean birth rate is significantly lower compared to the others. This is an indication that this time our simulations are overestimating the number of detected X-ray emitting neutron stars compared to reality. However while overestimating the numbers for the entire X-ray detected population, these simulations predict 10 ± 4 young magnetars and 6 ± 3 XDINS-like sources allowing a better agreement with the real observed numbers, i.e., 7 and 7 respectively.

In Fig. 8 we compare the $\log N - \log S$ distributions. In the left panel we show the distribution when considering only the young magnetars and XDINS-like sources. In this case, the observed $\log N - \log S$ falls inside the 1- σ uncertainty of the simulations. When considering the whole X-ray population (right panel) the simulations are compatible at 1- σ level with the high-flux tail of the observed distribution. On the other hand at lower fluxes,

while being still compatible with the observed distribution at a 3- σ level, the simulations predict more sources at flux values between $10^{-14} - 10^{-12} \text{ erg s}^{-1} \text{ cm}^{-2}$. This excess is also reflected in the $P - \dot{P}$ diagram where the number of mock detected sources with fluxes in this range but with spin periods in the range between 10 to 100 s is overestimated, as highlighted above. Nevertheless, it is important to note that the simulations are able to reproduce the tail at high fluxes where young or nearby bright sources dominate and where the completeness level of the observed sample is higher.

In Fig. 9 we show the best fit distribution for the initial magnetic fields together with its uncertainty. In particular we draw 10000 values from the posterior distribution obtained from round 5 (see Fig. 6) and evaluate the median distribution (purple solid lines) and the 1 σ and 3 σ uncertainties (dashed regions).

6. DISCUSSION

Compared with the results on radio pulsars obtained in Pardo-Araujo et al. (2025), here we find that the initial spin period distribution is shifted to larger values even if the values are consistent within the uncertainties. The uncertainty on the parameters describing this distribution is still large and indicates that these parameters are difficult to constrain as already discussed in previous works. The memory of the initial spin periods is rapidly lost during the magneto-rotational evolution. Adding the sample of X-ray emitting neutron stars at higher magnetic field values does not help in these regards as the stronger the magnetic field the faster is the evolution in the $P - \dot{P}$ diagram.

As $\mu_{\log P}$ is negatively correlated with the initial magnetic field parameters (see Fig. 6), an initial spin period distribution shifted to larger values allows for lower values of $\mu_{\log B,1}$. Therefore the first gaussian component of the magnetic field distribution is shifted to slightly lower values compared to Graber et al. (2024); Pardo-Araujo et al. (2025). This is also compensated by the addition of the second component at stronger magnetic fields that helps providing sources with magnetic fields above 10^{13} G that can be detected as radio pulsars (see Fig. 9).

As in Pardo-Araujo et al. (2025) we find a slightly negative correlation between the radio luminosity parameter, $\mu_{\log L_0}$, and $\mu_{\log P}$, and a slightly positive correlation between $\mu_{\log L_0}$ and $\mu_{\log B,1}$. This means that as the radio pulsar population shifts to the right and to the bottom of the $P - \dot{P}$ diagram because of a larger $\mu_{\log P}$ and a smaller $\mu_{\log B,1}$ respectively, the radio luminosity can also be slightly smaller as otherwise too many pulsars with low rotational energy would be detected.

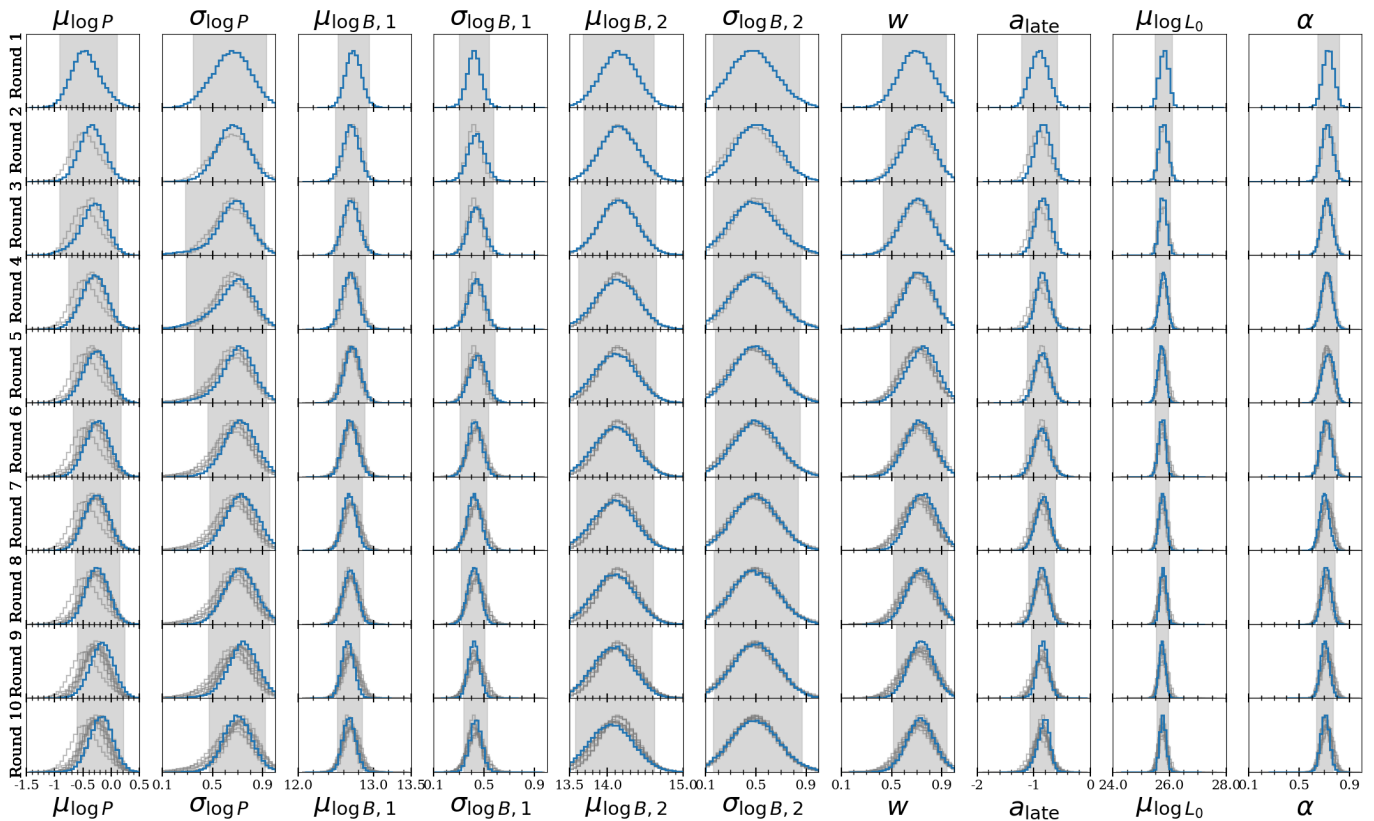


Figure 5. Results of the TSNPE algorithm applied to our population synthesis where we assumed a double log-normal initial magnetic field distribution. Each row shows the marginalized posterior obtained in each round of inference where the columns refers to different parameters. The last column shows the coverage probability computed on the test dataset. This is only computed in the first round. In each panel, for a given parameter the marginalized posterior computed in that specific round is shown in blue, while the marginalized posteriors from previous rounds are shown in light gray. The gray shaded area represents the 95% credibility interval of the approximated posterior for that round. In each of these 1-D marginal posterior distribution, the horizontal axes represent the parameters' prior ranges.

1066 Turning to the parameters relevant for the X-ray pop-
 1067 ulation, we find that when inferring on the entire sam-
 1068 ple of X-ray emitting neutron stars, the second com-
 1069 ponent of the initial magnetic field is centered at values of
 1070 $\sim 7 \times 10^{13}$ G. On the other hand when focusing the
 1071 inference on the sub-populations of young magnetars
 1072 and XDINSs the mean value of this component shifts
 1073 to $\sim 1 \times 10^{14}$ G. This difference is due to the fact that
 1074 in the first case, when fitting the entire observed X-ray
 1075 population, the TSNPE algorithm tries to reproduce the
 1076 spin period distribution which shows a clear cut off at
 1077 periods of around $\sim 10-20$ s. To achieve this, the initial
 1078 magnetic field cannot be too large, otherwise, the spin-
 1079 down would be too strong, leading to final spin periods
 1080 larger than those observed. However, by limiting the
 1081 initial magnetic field strength the simulations poorly re-
 1082 produce the high \dot{P} values of the young magnetars as can
 1083 be seen by looking at the pink contour lines and crosses
 1084 in Fig. 3. Moreover, another counter effect is the reduction
 1085 of the X-ray luminosities and the observed fluxes,

1086 which is indeed evident in the $\log N - \log S$ distribution
 1087 (see Fig. 4). On the other hand, when focusing the in-
 1088 ference on the young magnetars and XDINSs, a second
 1089 component with stronger initial magnetic fields can re-
 1090 produce both sub-populations. This implies also higher
 1091 thermal luminosities and a better fit to the high-flux tail
 1092 of the $\log N - \log S$ distribution (see Fig. 8). However,
 1093 the resulting population of X-ray emitting neutron stars
 1094 tends to have spin periods longer than those observed
 1095 due to a stronger spin-down (see Fig. 7).

1096 In general the uncertainty on the values of the pa-
 1097 rameters describing the second component of the initial
 1098 magnetic field distribution is large as can be observed
 1099 by the large variance associated to this component in
 1100 Fig. 9. This is a consequence of the low number statis-
 1101 tics for the X-ray emitting neutron stars (see also Ap-
 1102 pendix B). This can indeed introduce random statistical
 1103 noise in the maps of the simulated and observed samples
 1104 which makes the training process more challenging and
 1105 the inference results less precise. On the other hand this

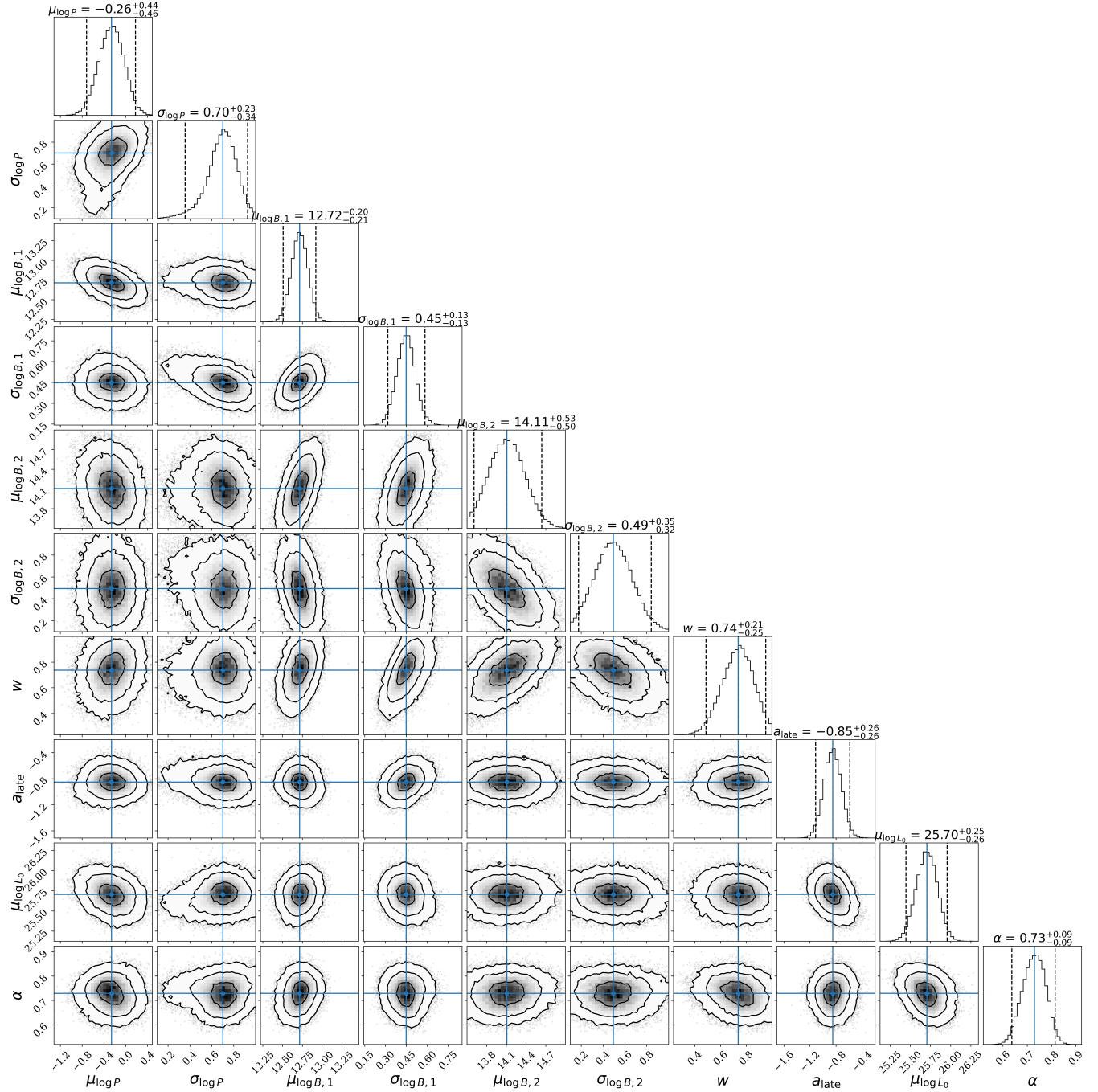


Figure 6. Corner plot of the posterior distribution conditioned on the observed data restricted to the radio pulsars and the sub-populations of young magnetars and XDINSs. The posterior is estimated from the round 5 of the TSNPE algorithm and adopted for the best parameter estimation in Section 5.2.

1106 could be also an indication that the chosen parametrisation describing the shape of the initial magnetic field
 1107 distribution or the adopted models for the evolution of
 1108 magnetar-like sources in the $P-\dot{P}$ diagram or the obser-
 1109 vational biases are not describing faithfully the reality.

1111 6.1. The ~ 20 s cut-off in the magnetar population

1112 The presence of a cut-off in the observed spin pe-
 1113 riod distribution at around ~ 20 s is intriguing and it
 1114 has been challenging to explain in previous population
 1115 synthesis studies (see for example Gullón et al. 2015).
 1116 The fact that also our models struggle to reproduce this
 1117 sharp feature could be due to different aspects.

1118 First of all our treatment of the outburst rate is sim-
 1119 plified, primarily as we rely on 2D magneto-thermal sim-

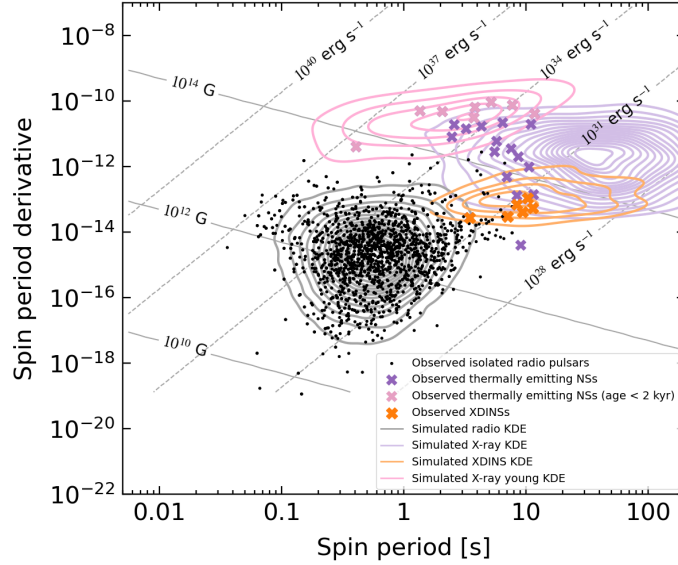


Figure 7. Comparison in the $P - \dot{P}$ diagram between the observed population of radio pulsars and X-ray emitting neutron stars and the best simulated populations assuming a double log-normal initial magnetic field distribution. Points and crosses represent the observed radio pulsars and X-ray emitting neutron stars. Pink crosses represents the young (estimated ages lower than 2 kyr) magnetars, while orange crosses represent the observed XDINSs. The contour lines represent density contours obtained from 100 simulations generated from sets of input parameters drawn from the posterior distribution obtained from round 5.

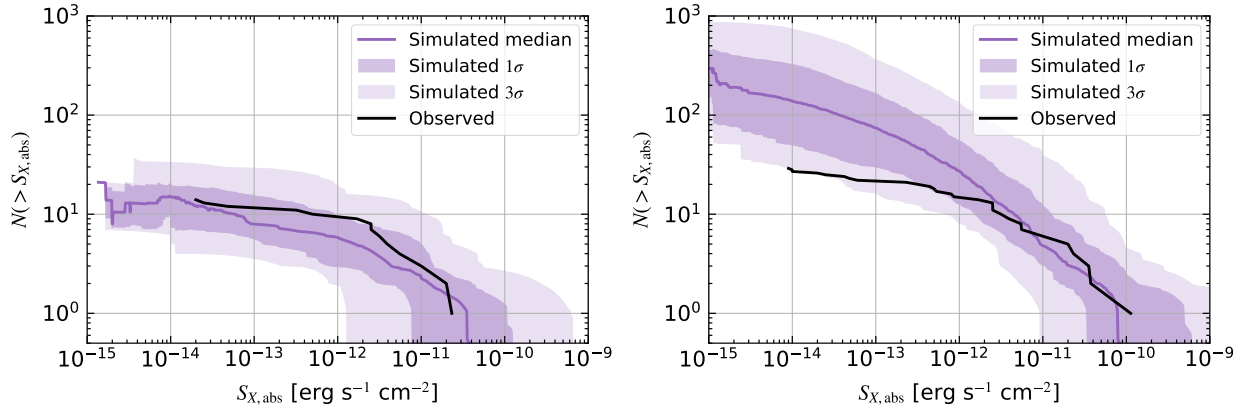


Figure 8. Comparison of the $\log N - \log S$ distributions for the observed and simulated X-ray thermally emitting neutron stars assuming a double log-normal initial magnetic field distribution. The left panel considers only the young magnetars (with age lower than 2 kyr) and XDINS-like sources. The right panel represents the entire observed X-ray population. In both plots the black line represents the trend for the observed population while the purple line and bands represent the median, the $1\text{-}\sigma$ and $3\text{-}\sigma$ uncertainties computed over 100 simulations generated from sets of parameters drawn from the posterior distribution obtained from round 5.

1120 ulations where failures are obtained under simplified as-
 1121 sumptions (see [Dehman et al. 2020](#), for more details),
 1122 secondly as we consider that all crust failures events
 1123 lead to a detectable outburst. This picture does not
 1124 take into account the energy of these events and their
 1125 luminosity in gamma-ray and X-ray photons. Quan-
 1126 tifying the efficiency with which the energy dissipated
 1127 by the stresses is converted into photon luminosity that
 1128 could be detected by gamma-ray and X-ray instruments
 1129 is challenging ([Lander 2023](#); [Qu & Bransgrove 2026](#)).
 1130 Moreover we are not taking into account sensitivities

1131 and limitations of current and past X-ray observatories
 1132 for transient detection. One issue for example is that
 1133 outbursts occurring during periods when the source is
 1134 Sun-constrained, i.e., too close to the Sun to be ob-
 1135 served, will be missed. This happens for a few months
 1136 each year for every source effectively reducing the de-
 1137 tectability time-window; Therefore, combining all these
 1138 aspects, in our simulations we are likely overestimating
 1139 the number of sources that could be detectable due to
 1140 an outburst event and this could also lead to an over-

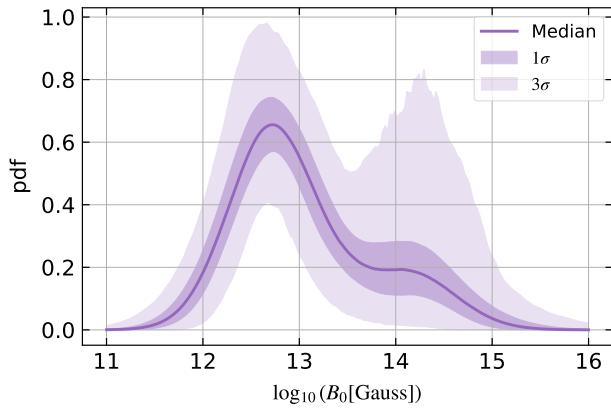


Figure 9. Best fit distribution of initial magnetic fields for the inference experiment on radio pulsars, young magnetars and XDINS. The purple solid line represents the median value while the shaded regions represents the 1σ and 3σ uncertainties computed over 10000 random samples of the posterior distribution shown in Fig. 6.

1141 detection of sources at long spin periods which have not
1142 been observed in reality.

1143 A second aspect to consider is that our results rely
1144 on the assumption that the configuration of the initial
1145 magnetic field has only a dipolar poloidal and toroidal
1146 components. For the magnetar population this could
1147 not hold, the presence of strong multipole components
1148 beside the dipole (Dehman et al. 2023b, e.g.) could af-
1149 fect how the magnetic field evolves, implying a faster
1150 decay and an enhanced dissipation in the neutron star
1151 crust that could lead to higher X-ray luminosities in the
1152 first stages of the magnetar evolution. A faster decay
1153 could help explain the sharp drop of sources at a spin
1154 period of ~ 20 s as the spin-down evolutionary trajec-
1155 tory would bend down sooner in the $P - \dot{P}$ diagram. A
1156 different configuration of the field also affects the rate of
1157 expected crustal failures and consequently of outburst
1158 events. The presence of strong multipolar components
1159 in general should enhance the stresses in the crust and
1160 the rate of failures leading to more outburst events and
1161 a greater number of detectable magnetars.

1162 A second aspect could be related to the evolution-
1163 ary models. In the case of young magnetars their fre-
1164 quent flares and outburst activity could cause changes in
1165 the magnetosphere configuration and particle winds that
1166 could momentarily enhance the spin-down rate (Tong
1167 et al. 2013; Pétri 2019). In this case assuming a force-
1168 free dipolar magnetospheric spin-down model could be
1169 an over-simplification and could bias the estimate of the
1170 surface dipolar magnetic field of young magnetars and
1171 therefore their birth properties. A different evolution-
1172 ary track in the $P - \dot{P}$ diagram where the \dot{P} is enhanced
1173 could also contribute to explain the timing properties of

1174 magnetars. However an enhanced spin-down acting for
1175 long time would lead to longer final spin periods which
1176 would be against the observed cut-off at ~ 20 s. If the
1177 enhanced spin-down is only temporary this would imply
1178 that we are detecting magnetars only in this short tem-
1179 porary phase which would make such detections more
1180 unlikely unless a strong detection biases like an outburst
1181 event is present.

1182 6.2. Estimate of the magnetar fraction

1183 When inferring considering the entire X-ray popu-
1184 lation we find that the second component of the ini-
1185 tial magnetic field distribution has a relative weight of
1186 $17_{-16}^{+22}\%$. On the other hand when focusing on the young
1187 magnetars and XDINSs we find $26_{-21}^{+25}\%$. This number
1188 can also be interpreted as the fraction of neutron stars
1189 born with a strong magnetar-like magnetic field. These
1190 values are consistent within the uncertainties with the
1191 value $10.7_{-4.4}^{+18.8}\%$ inferred by Sautron et al. (2025) who
1192 performed a simulation based inference study although
1193 only considering magnetars and with the estimates of
1194 Pardo-Araujo et al. (2026) who put constraints on the
1195 fraction of neutron stars born as magnetars by com-
1196 bining the young population of neutron stars and their
1197 supernova association, CCOs and XDINSs. While using
1198 the same simulation framework and similar assumptions
1199 as in Pardo-Araujo et al. (2026) the approach here is
1200 slightly different as we focus on the entire evolved pop-
1201 ulation. This makes this study and results to be more
1202 sensitive to the modelling of the correct observational bi-
1203 ases and evolutionary scenarios. In Pardo-Araujo et al.
1204 (2026), we found a conservative range for the magne-
1205 tar fraction of 30–70%. Their Extended Data Figure
1206 4 shows that the inferred magnetar fraction decreases
1207 as the neutron star birth rate increases. Therefore, our
1208 lower estimated magnetar fraction is consistent with the
1209 higher birth rates we predict (3–4 neutron stars per cen-
1210 tury, see Eq. 21). Overall if we combine these estimates
1211 we can argue that most likely the Galactic neutron star
1212 birth rate lies in the range 3–4 neutron stars per century
1213 of which a fraction of ~ 30 –50% are born as magnetars.
1214 Constraints on the magnetar fraction are important to
1215 asses the impact of these progenitors as possible engines
1216 of extreme events such as FRBs (Beniamini et al. 2023,
1217 2025), superluminous supernovae (Inserra et al. 2013),
1218 as well as the plateau phases observed in many GRB
1219 afterglows (Metzger et al. 2011; Lü & Zhang 2014).

1220 6.3. The long-period pulsar subpopulation

1221 Recently a pulsar with a spin period of ~ 76 s (Caleb
1222 et al. 2022) and several Long Period Transients (LPTs),
1223 recurring on timescales ranging from hundreds of sec-
1224 onds up to several hours, have been discovered in radio

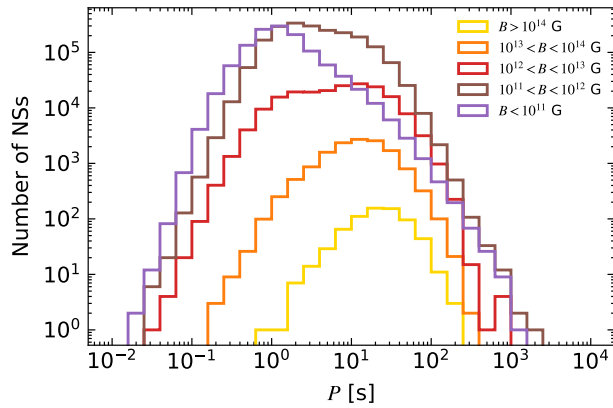


Figure 10. Distribution of the final spin period of the entire evolved neutron star population as a function of different ranges of final magnetic fields.

(see Rea et al. 2026, for a review). Neutron stars and in particular magnetars have been suggested as possible engines to produce the emission of some of these LPTs. In the assumptions of our best models, in order to see how many neutron stars we expect in our Galaxy to have ultra-long spin period we performed a simulation adopting the best parameter values inferred in Section 5.2. To simulate the full population we assume a birth rate of 3.5 neutron stars per century and evolve it up to a maximum age of 10^8 yrs for a total of 3.5×10^6 neutron stars. Note that the birth rate value we consider here is consistent with the values obtained in Section 5.2. In Fig. 10 we report histograms of the final spin periods considering different ranges of final magnetic fields for the entire population. We predict that the total number of sources with spin periods above 20s should be $\sim 2 \times 10^5$ sources ($\sim 6\%$ of the entire population) with ~ 400 objects ($\sim 0.01\%$) with still magnetar-like magnetic fields above 10^{14} G. In particular we expect the number of neutron stars with spin periods above 100 s to be ~ 5000 sources ($\sim 0.1\%$). We note that in our simulation framework neutrons stars with spin periods longer than a few seconds becomes hard to detect. This is due to a combination of factors. First of all we assume a radio beam aperture which as an inverse dependence on the spin period as $\propto P^{-1/2}$ (see Eq. 13 in Graber et al. 2024, and references therein). Moreover neutron star reaching long spin periods are usually the ones with stronger magnetic fields and therefore a stronger tendency of evolving towards being aligned rotators, i.e. with magnetic field dipole axis aligned with the rotation axis (see Eq.(4)). These aspects naturally reduce the probability of the radio beam intersecting our line of sight for slow rotators. Furthermore without considering alternative evolutionary spin-down models (see, e.g., Ronchi et al. 2022; Gençali & Ertan 2024; Zhou et al.

2024) and assuming dipolar spin-down only, we predict that very few sources could reach spin periods around 1000 s. Therefore without other mechanism to enhance spin-down our models could explain only the fast spinning end of the LPT population.

6.4. The source populations of FRBs

There is broad and convincing evidence that FRBs are emitted by young, energetic neutron stars (e.g., Pastor-Marazuela et al. 2025). As the bursts are, on average, 10^{12} times brighter than normal pulsars (cf. van Leeuwen et al. 2023), the inferred energy budget suggests that magnetars, specifically, could be emitting these bursts. The case is strengthened by both single-object and population evidence: the detection of a short bright burst from magnetar SGR 1935+2154 (Bochenek et al. 2020), the agreement in burst wait-time statistics between specific repeaters and magnetars (e.g. Wadiasingh & Timokhin 2019), and the finding that the number density, spectral index and dispersion measures of the population of FRBs agrees qualitatively with the expectations for a magnetar origin (Gardenier & van Leeuwen 2021). The population synthesis method we described here has the potential to make this link much more quantitative. By connecting our radio and X-ray results to the state-of-the-art in FRB population synthesis codes (e.g. Wang & van Leeuwen 2024) we will be able to determine, for example, if FRB repetition frequency, too, is guided by the same outburst prescriptions that drive magnetar flares (Sect. 3.5, and bottom panel of Fig. 1). Such a detection would offer strong evidence that FRBs are, indeed, distant magnetars.

7. CONCLUSIONS

We performed a simulation based inference study to constrain the Galactic population of neutron stars. Our approach was unique in constructing a unified framework for the populations of radio pulsars, magnetars, and XDINs with a significant thermal component in their spectra. To achieve this we developed ML-Poppyns, a population synthesis framework that combines models to simulate the birth, evolution and detection of a Galactic population of neutron stars, with simulation based inference that exploit the power of neural networks to perform parameter inference. To reproduce the properties of magnetars and XDINs, we incorporate results from state-of-the-art 2D magneto-thermal simulations to model the coupled evolution of magnetic fields, surface temperature and crustal failures.

Using these, we determine which source population best describes the observed one. This underlying population can help refine the expected detection numbers

1311 for future instruments like the Square Kilometer Array
 1312 (SKA Keane et al. 2015, 2025) in the radio band and
 1313 eXTP (Santangelo et al. 2019) and NewAthena (Cruise
 1314 et al. 2025) in the X-ray band. It also can serve as a
 1315 starting point for investigating the impact of strongly
 1316 magnetic neutron stars as central engines for powerful
 1317 events such as FRBs and GRBs.

1318 We show that an initial magnetic field distribution
 1319 described by two log-normal components with means of
 1320 5×10^{12} G and 1×10^{14} G respectively, is able to repro-
 1321 duce the properties of radio pulsars, young magnetars
 1322 and XDINSs. It does, however, struggle to explain the
 1323 absence of detected sources with spin periods larger than
 1324 ~ 20 s. We also find that to simultaneously explain the
 1325 detected numbers at both electromagnetic wavelengths,
 1326 we require a Galactic neutron star birth rate of 3-4 neu-
 1327 tron stars per century, with a 10-50% magnetar fraction.

1328 M.R. and J.v.L. are supported by the Dutch
 1329 Research Council (NWO) via the grant CORTEX
 1330 (NWA.1160.18.316) of the research programme NWA-
 1331 ORC. V.G. is supported by a UKRI Future Leaders Fel-
 1332 lowship (grant number MR/Y018257/1). C.P.A. and
 1333 N.R. are supported by the ERC via the Consolidator
 1334 grant “MAGNESIA” (No. 817661), the ERC Proof of
 1335 Concept “DeepSpacePULSE” (No. 101189496), and by
 1336 the program Unidad de Excelencia María de Maeztu
 1337 CEX2020-001058-M. We also acknowledge support from
 1338 the Catalan grant SGR2021-01269 (PI: Graber/Rea)
 1339 and the Spanish grant PID2023-153099NA-I00 (PI: Coti
 1340 Zelati). C.P.A.’s work has been carried out within
 1341 the framework of the doctoral program in Physics at
 1342 the Universitat Autònoma de Barcelona. C.D. is sup-
 1343 ported by the Ministerio de Ciencia, Innovación y
 1344 Universidades (JDC2023-052227-I), co-funded by AEI
 1345 (MCIN/AEI/10.13039/501100011033), the FSE+, and
 1346 the Universidad de Alicante, and also acknowledges
 1347 support from the Conselleria d’Educació, Cultura,
 1348 Universitats i Ocupació de la Generalitat Valenciana
 1349 (grant CIPROM/2022/13) and the AEI grant PID2021-
 1350 127495NB-I00. D.D.G. is supported by a Juan de la
 1351 Cierva fellowship (JDC2023-052264-I).

1352 The data production, processing, and analysis tools
 1353 for this paper have been implemented and operated
 1354 at the Port d’Informació Científica (PIC) data center.
 1355 PIC is maintained through a collaboration of the In-
 1356 stitut de Física d’Altes Energies (IFAE) and the Cen-
 1357 tro de Investigaciones Energéticas, Medioambientales y
 1358 Tecnológicas (Ciemat). We particularly thank Christian
 1359 Neissner and Martin Børstad Eriksen for their support
 1360 at PIC.

1361 We made use of the pulsar population synthesis code
 1362 ML-Poppyns Ronchi et al. (2021); Graber et al. (2024);
 1363 Pardo-Araujo et al. (2025) funded by the European Re-
 1364 search Council via the ERC Consolidator grant “MAG-
 1365 NESIA” (No. 817661; PI: N. Rea), and publicly avail-
 1366 able at [https://ice-csic-astroexotic.github.io/code/ml-](https://ice-csic-astroexotic.github.io/code/ml-poppyns/)
 1367 [poppyns/](https://ice-csic-astroexotic.github.io/code/ml-poppyns/).

1368 The authors thank Roberto Turolla for useful ex-
 1369 changes on the X-ray emission and resonant cyclotron
 1370 scattering and Emilie Parent for useful discussions on
 1371 the radio detection.

1372 *Software:* Astropy (Astropy Collaboration et al.
 1373 2013, 2018), healpy (Górski et al. 2005; Zonca et al.
 1374 2019), IPython (Perez & Granger 2007), JupyterLab,
 1375 Matplotlib (Hunter 2007), Numba (Lam et al. 2015),
 1376 NumPy (Oliphant 2006; van der Walt et al. 2011; Har-

ris et al. 2020), Pandas (McKinney 2010), PyGEDM, SciPy (Jones et al. 2001; Virtanen et al. 2020),
 PyTorch (Paszke et al. 2019), sbi (Tejero-Cantero et al. 2020) Sphinx.

APPENDIX

A. RESONANT CYCLOTRON SCATTERING

The non-relativistic classical resonant scattering cross section can be approximated as (see Canuto et al. 1971; Nobili et al. 2008; Yamasaki et al. 2020):

$$\sigma_{\text{res}}(\omega) \sim \pi^2 \frac{e^2}{m_e c} \delta(\omega - \omega_B)(1 + \cos^2 \theta), \quad (\text{A1})$$

where θ is the angle between the photon trajectory and the direction of the magnetic field line.

The effectiveness of the process is quantified by the resonant scattering optical depth τ_{res} which can be estimated by the integral:

$$\begin{aligned} \tau_{\text{res}} &= \int n_e \sigma_{\text{res}}(\omega) dl \\ &\sim \int_{R_{\text{NS}}}^r n_e \sigma_{\text{res}}(\omega) dr' \\ &= \frac{\pi^2 e^2 n_e}{m_e c} (1 + \cos^2 \theta) \int_{R_{\text{NS}}}^r \delta(\omega - \omega_B(r')) dr' \\ &= \frac{\pi^2 e^2 n_e}{m_e c} (1 + \cos^2 \theta) \frac{r}{3\omega_B} \\ &= \tau_0 (1 + \cos^2 \theta), \end{aligned} \quad (\text{A2})$$

where the integral is performed along the line of sight l , for simplicity taken to be the radial distance r from the star surface, n_e is the density of the magnetospheric plasma (assumed to be constant), and τ_0 :

$$\tau_0 = \frac{\pi^2 e^2 n_e r}{3m_e c \omega_B}. \quad (\text{A3})$$

Note that ω_B depends on the distance r since in the simplifying assumption of a poloidal dipole field we have that $B(r) \sim B_P R_{\text{NS}}^3 / r^3$ where B_P is the magnetic field strength at the pole. Therefore to solve the integral we used the property of the Dirac delta function:

$$\int_{-\infty}^{+\infty} \delta(f(x)) dx = \sum_i \frac{1}{|f'(x_i)|}, \quad (\text{A4})$$

where x_i are the zeros of the function $f(x)$. In our case $f(x)$ is $\omega - \omega_B(r)$ and its derivative with respect to r is $3\omega_B/r$. The zeros of our function are the values of the radial distance r where $\omega_B(r) = \omega$, i.e., where the frequency of the photon matches the cyclotron frequency.

To compute the spectrum distorted by resonant cyclotron scattering we used the simplified semi-analytical 1D model described in Lyutikov & Gavril (2006) (see also Rea et al. 2008). In this model it is assumed that the seed thermal photons coming from the surface propagate in the radial direction. They interact with the magnetospheric electron-positron plasma where particles are gyrating along the magnetic field lines and are assumed to have a top-hat thermal velocity distribution centered at zero and extending up to velocities $\pm\beta_T$. For simplicity it is assumed that photons propagate parallel to the magnetic field lines, either away or towards the star, hence in Eq.(A2), $\cos \theta = \pm 1$ and $\tau_{\text{res}} = 2\tau_0$. A photon with a given energy $E_0 = \hbar\omega_0$ will resonantly interact with electrons that are gyrating with a cyclotron frequency that matches their energy. This will define the distance from the star r where the interaction will happen. The probabilities that a photon with energy $E_0 = \hbar\omega_0$ undergoes resonant scattering and is transmitted or reflected are given by Eqs.(35) in Lyutikov & Gavril (2006) which we report here:

$$\begin{aligned}
1414 \quad p_+(\eta)d\eta &= e^{-\tau_0/2} \left[\delta(\eta) + \frac{\tau_0}{8\beta_T} \sqrt{\frac{4\beta_T - \eta}{\eta}} I_1 \left(\frac{\tau_0}{4\beta_T} \sqrt{\eta(4\beta_T - \eta)} \right) \right] d\eta, & (A5) \\
1415 \quad p_-(\xi)d\xi &= \frac{\tau_0}{8\beta_T} e^{-\tau_0/2} I_0 \left(\frac{\tau_0}{4\beta_T} \sqrt{(2\beta_T - \xi)(\xi + 2\beta_T)} \right) d\xi,
\end{aligned}$$

1416 where $\eta = (E - E_0)/E_0$ and $\xi = (E_0 - E)/E_0$ and E represents the energy of the scattered photon. Rewriting the
1417 probabilities above in terms of the energies gives the expressions (see Eq.(36) in [Lyutikov & Gavriil 2006](#)):

$$\begin{aligned}
1418 \quad p_+(E, E_0)dE_0 &= e^{-\tau_0/2} \left[\delta(E - E_0) + \frac{\tau_0}{8\beta_T E_0} \sqrt{\frac{4\beta_T E_0 - E + E_0}{E - E_0}} \right. & (A6) \\
1419 \quad &\left. I_1 \left(\frac{\tau_0}{4\beta_T E_0} \sqrt{(E - E_0)(4\beta_T E_0 - E + E_0)} \right) \right] dE_0,
\end{aligned}$$

$$\begin{aligned}
1420 \quad p_-(E, E_0)dE_0 &= \frac{\tau_0}{8\beta_T E_0} e^{-\tau_0/2} & (A7) \\
1421 \quad &I_0 \left(\frac{\tau_0}{4\beta_T E_0} \sqrt{(2\beta_T E_0 - E_0 + E)(E_0 - E + 2\beta_T E_0)} \right) dE_0,
\end{aligned}$$

1422 From the plots in Fig. 2 in [Lyutikov & Gavriil \(2006\)](#) a photon that is reflected can both gain or lose energy. Since
1423 the dipolar magnetic field decays as $\sim r^{-3}$, the cyclotron frequency of electrons gyrating along the magnetic field lines
1424 also decreases as $\sim r^{-3}$ as one moves far away from the star surface. Therefore if a photon is resonantly scattered and
1425 reflected back towards the stellar surface it could interact again with the electron plasma only if it gains energy. If this
1426 happens it can be transmitted again towards the observer. Since in the transmission the photon only gain energy, as
1427 it propagates far away from the star it will not interact again with electrons since they will have cyclotron frequencies
1428 below its energy.

1429 These probabilities depends on two free parameters, i.e., τ_0 and β_T . Following [Gullón et al. \(2015\)](#) we assumed that
1430 these two parameters depends on the dipolar magnetic field strength B of the neutron star according to the following
1431 scaling relations:

$$1432 \quad \tau_0 = \begin{cases} 0.001 & \text{if } B \leq 10^{13} \text{ G} \\ \frac{B}{10^{14} \text{ G}} & \text{if } B > 10^{13} \text{ G} \end{cases} & (A8)$$

$$1434 \quad \beta_T = \begin{cases} 0.001 & \text{if } B \leq 10^{13} \text{ G} \\ 0.3 & \text{if } B > 10^{13} \text{ G}. \end{cases} & (A9)$$

1435 This approximated relations roughly reproduce the correlations between τ_0 , β_T and B found in [Rea et al. \(2008\)](#).

1436 If $n_{\text{BB}}(E_0) = I_{\text{BB}}(E_0)/E_0$ is the thermal spectrum coming from the neutron star surface in number of photons,
1437 where

$$1438 \quad I_{\text{BB}}(E) = \frac{2}{h^3 c^2} \frac{E^3}{e^{\frac{E}{k_B T_\infty}} - 1}, & (A10)$$

1439 is a black-body intensity spectrum, the resulting photon intensity spectrum $n_{\text{RCS}}(E)$ due to cyclotron resonant scat-
1440 tering can be computed by summing various contributions coming from various reflection events:

$$\begin{aligned}
1441 \quad n_{\text{RCS}}(E) &= \int dE_0 p_+(E, E_0) n_{\text{BB}}(E_0) + & (A11) \\
1442 \quad &+ \int dE_1 p_+(E, E_1) \int dE_0 p_-(E_1, E_0) n_{\text{BB}}(E_0) + \\
1443 \quad &+ \int dE_3 p_+(E, E_3) \int dE_2 p_-(E_3, E_2) \int dE_1 p_-(E_2, E_1) \\
1444 \quad &\dots
\end{aligned}$$

1445 This sum quickly converges and for numerical purposes we will consider 6 reflection terms (see [Lyutikov & Gavriil](#)
1446 [2006](#)).

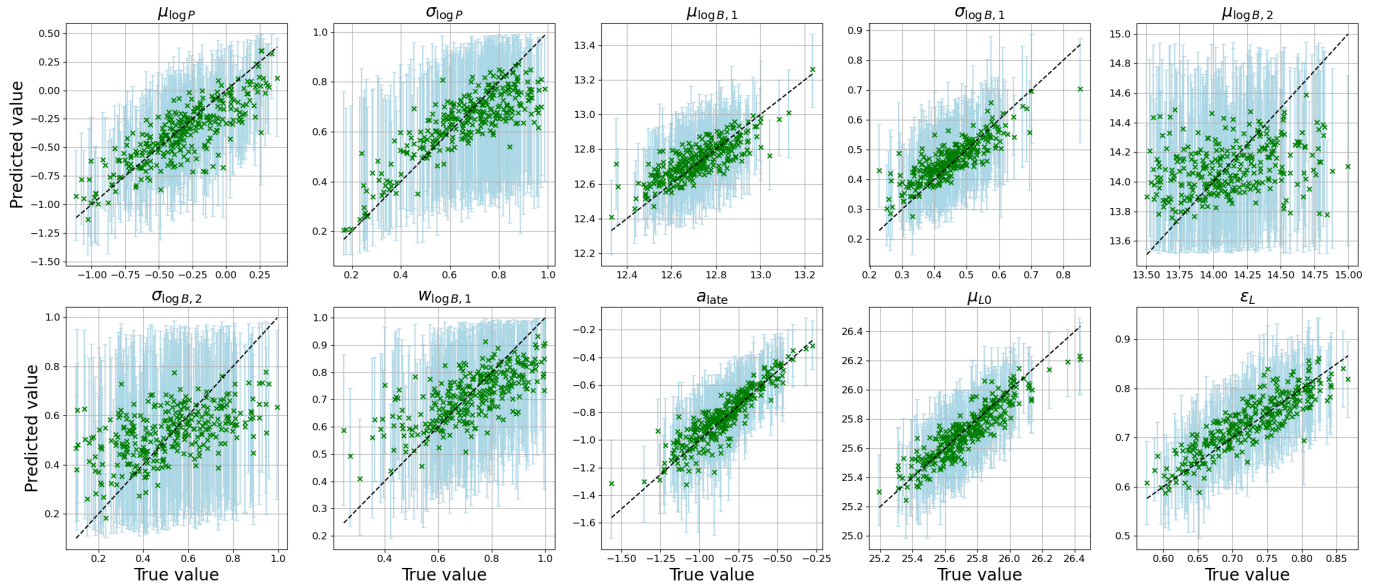


Figure 11. Results of the predictive check test performed on a test dataset of 300 simulations using the density estimator trained on radio pulsars and the sub-populations of young magnetars and XDINs. We used the density estimator obtained from round 5 (see also Fig. 5). For each parameter, we display the predicted values and their uncertainties, i.e., the median values (green crosses) and the 95% confidence interval (light blue error bars) of the posterior distribution, versus the true value as green crosses and light blue error bars respectively.

1447

B. PREDICTIVE CHECK AND COVERAGE TEST

1448 To evaluate the reliability of the trained posterior estimator in round 5 of Section 5.2 we check its performance on a
 1449 test dataset of 300 simulations drawn from the proposal restricted prior. In Fig. 11 we show the inference results on
 1450 the test dataset for each of the 10 parameters we are inferring. For each test sample we report the median value and
 1451 the 95% credible interval from the predicted posterior distribution and we compare it with the ground truth value. As
 1452 can be seen by the scatter and uncertainties in the predicted values, the parameters related to the second component
 1453 of the initial magnetic field, $\mu_{\log B,2}$ and $\sigma_{\log B,2}$ are difficult to constrain. We also performed the coverage probability
 1454 test (Cook et al. 2006; Hermans et al. 2021) on the trained estimator after the first round of TSNPE. To do this we use
 1455 the 300 test samples and compute the percentage of ground truth values that fall inside a given credibility level of the
 1456 corresponding estimated posteriors. The coverage plot shows that the posterior estimator is overall conservative, i.e.,
 1457 the coverage line lies well above the diagonal (see also Graber et al. 2024; Pardo-Araujo et al. 2025, for an explanation
 1458 of the coverage probability).

REFERENCES

- 1459 Archibald, R. F., Kaspi, V. M., Tendulkar, S. P., & Scholz,
 1460 P. 2016, ApJL, 829, L21,
 1461 doi: [10.3847/2041-8205/829/1/L21](https://doi.org/10.3847/2041-8205/829/1/L21)
- 1462 Ascenzi, S., Viganò, D., Dehman, C., et al. 2024, MNRAS,
 1463 533, 201, doi: [10.1093/mnras/stae1749](https://doi.org/10.1093/mnras/stae1749)
- 1464 Astropy Collaboration, Robitaille, T. P., Tollerud, E. J.,
 1465 et al. 2013, A&A, 558, A33,
 1466 doi: [10.1051/0004-6361/201322068](https://doi.org/10.1051/0004-6361/201322068)
- 1467 Astropy Collaboration, Price-Whelan, A. M., Sipőcz, B. M.,
 1468 et al. 2018, AJ, 156, 123, doi: [10.3847/1538-3881/aabc4f](https://doi.org/10.3847/1538-3881/aabc4f)
- 1469 Balucinska-Church, M., & McCammon, D. 1992, ApJ, 400,
 1470 699, doi: [10.1086/172032](https://doi.org/10.1086/172032)
- 1471 Barrère, P., Guilet, J., Reboul-Salze, A., Raynaud, R., &
 1472 Janka, H.-T. 2022, A&A, 668, A79,
 1473 doi: [10.1051/0004-6361/202244172](https://doi.org/10.1051/0004-6361/202244172)
- 1474 Barret, D., & Dupourqué, S. 2024, arXiv e-prints,
 1475 arXiv:2401.06061, doi: [10.48550/arXiv.2401.06061](https://doi.org/10.48550/arXiv.2401.06061)
- 1476 Becker, W., & Truemper, J. 1997, A&A, 326, 682,
 1477 doi: [10.48550/arXiv.astro-ph/9708169](https://doi.org/10.48550/arXiv.astro-ph/9708169)
- 1478 Beloborodov, A. M. 2009, ApJ, 703, 1044,
 1479 doi: [10.1088/0004-637X/703/1/1044](https://doi.org/10.1088/0004-637X/703/1/1044)
- 1480 —. 2013, ApJ, 762, 13, doi: [10.1088/0004-637X/762/1/13](https://doi.org/10.1088/0004-637X/762/1/13)
- 1481 Beniamini, P., Wadiasingh, Z., Hare, J., et al. 2023,
 1482 MNRAS, 520, 1872, doi: [10.1093/mnras/stad208](https://doi.org/10.1093/mnras/stad208)

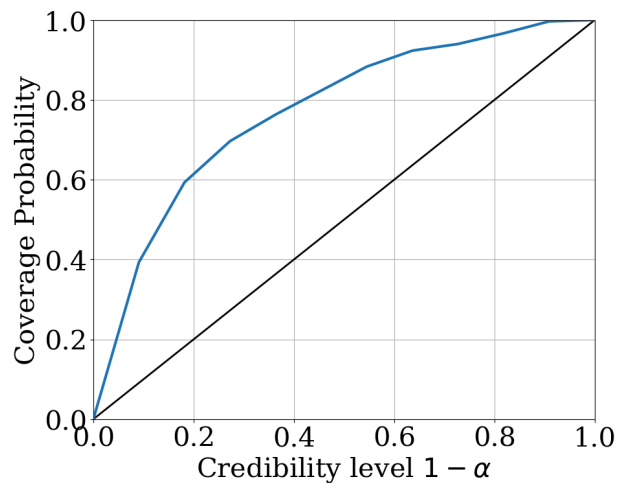


Figure 12. Coverage diagnostic plot for the posterior estimator trained on radio pulsars and the sub-populations of young magnetars and XDINSs from round 5.

- 1483 Beniamini, P., Wadiasingh, Z., Trigg, A., et al. 2025, *ApJ*,
1484 980, 211, doi: [10.3847/1538-4357/ada947](https://doi.org/10.3847/1538-4357/ada947)
- 1485 Bochenek, C. D., Ravi, V., Belov, K. V., et al. 2020,
1486 *Nature*, 587, 59, doi: [10.1038/s41586-020-2872-x](https://doi.org/10.1038/s41586-020-2872-x)
- 1487 Borghese, A., & Esposito, P. 2023, in *Handbook of X-ray
1488 and Gamma-ray Astrophysics*, 146,
1489 doi: [10.1007/978-981-16-4544-0_102-1](https://doi.org/10.1007/978-981-16-4544-0_102-1)
- 1490 Bradt, H. V., Rothschild, R. E., & Swank, J. H. 1993,
1491 *A&AS*, 97, 355
- 1492 Caleb, M., Heywood, I., Rajwade, K., et al. 2022, *Nature
1493 Astronomy*, 6, 828, doi: [10.1038/s41550-022-01688-x](https://doi.org/10.1038/s41550-022-01688-x)
- 1494 Camilo, F., Ransom, S. M., Halpern, J. P., et al. 2006,
1495 *Nature*, 442, 892, doi: [10.1038/nature04986](https://doi.org/10.1038/nature04986)
- 1496 Canuto, V., Lodenquai, J., & Ruderman, M. 1971, *PhRvD*,
1497 3, 2303, doi: [10.1103/PhysRevD.3.2303](https://doi.org/10.1103/PhysRevD.3.2303)
- 1498 Carrasco, F., Viganò, D., Palenzuela, C., & Pons, J. A.
1499 2019, *MNRAS*, 484, L124, doi: [10.1093/mnrasl/slz016](https://doi.org/10.1093/mnrasl/slz016)
- 1500 Carreau, T., Fantina, A. F., & Gulminelli, F. 2020, *A&A*,
1501 640, A77, doi: [10.1051/0004-6361/202038347](https://doi.org/10.1051/0004-6361/202038347)
- 1502 Chugunov, A. I., & Horowitz, C. J. 2010, *MNRAS*, 407,
1503 L54, doi: [10.1111/j.1745-3933.2010.00903.x](https://doi.org/10.1111/j.1745-3933.2010.00903.x)
- 1504 Cieřlar, M., Bulik, T., & Osłowski, S. 2020, *MNRAS*, 492,
1505 4043, doi: [10.1093/mnras/staa073](https://doi.org/10.1093/mnras/staa073)
- 1506 Cook, S., Gelman, A., & Rubin, D. 2006, *Journal of
1507 Computational and Graphical Statistics*, 15,
1508 doi: [10.1198/106186006X136976](https://doi.org/10.1198/106186006X136976)
- 1509 Coti Zelati, F., Rea, N., Pons, J. A., Campana, S., &
1510 Esposito, P. 2018, *MNRAS*, 474, 961,
1511 doi: [10.1093/mnras/stx2679](https://doi.org/10.1093/mnras/stx2679)
- 1512 Cranmer, K., Brehmer, J., & Louppe, G. 2020, *Proceedings
1513 of the National Academy of Science*, 117, 30055,
1514 doi: [10.1073/pnas.1912789117](https://doi.org/10.1073/pnas.1912789117)
- 1515 Cruise, M., Guainazzi, M., Aird, J., et al. 2025, *Nature
1516 Astronomy*, 9, 36, doi: [10.1038/s41550-024-02416-3](https://doi.org/10.1038/s41550-024-02416-3)
- 1517 D’Aì, A., Evans, P. A., Burrows, D. N., et al. 2016,
1518 *MNRAS*, 463, 2394, doi: [10.1093/mnras/stw2023](https://doi.org/10.1093/mnras/stw2023)
- 1519 Dask Development Team. 2016, Dask: Library for dynamic
1520 task scheduling. <http://dask.pydata.org>
- 1521 Dax, M., Green, S. R., Gair, J., et al. 2021, *PhRvL*, 127,
1522 241103, doi: [10.1103/PhysRevLett.127.241103](https://doi.org/10.1103/PhysRevLett.127.241103)
- 1523 De Grandis, D., Taverna, R., Turolla, R., et al. 2021, *ApJ*,
1524 914, 118, doi: [10.3847/1538-4357/abfdac](https://doi.org/10.3847/1538-4357/abfdac)
- 1525 Dehman, C., Pons, J. A., Viganò, D., & Rea, N. 2023a,
1526 *MNRAS*, 520, L42, doi: [10.1093/mnrasl/slad003](https://doi.org/10.1093/mnrasl/slad003)
- 1527 Dehman, C., Viganò, D., Ascenzi, S., Pons, J. A., & Rea, N.
1528 2023b, *MNRAS*, 523, 5198, doi: [10.1093/mnras/stad1773](https://doi.org/10.1093/mnras/stad1773)
- 1529 Dehman, C., Viganò, D., Pons, J. A., & Rea, N. 2023c,
1530 *MNRAS*, 518, 1222, doi: [10.1093/mnras/stac2761](https://doi.org/10.1093/mnras/stac2761)
- 1531 Dehman, C., Viganò, D., Rea, N., et al. 2020, *ApJL*, 902,
1532 L32, doi: [10.3847/2041-8213/abbda9](https://doi.org/10.3847/2041-8213/abbda9)
- 1533 Deistler, M., Goncalves, P. J., & Macke, J. H. 2022, in
1534 *Advances in Neural Information Processing Systems*, ed.
1535 S. Koyejo, S. Mohamed, A. Agarwal, D. Belgrave,
1536 K. Cho, & A. Oh, Vol. 35 (Curran Associates, Inc.),
1537 23135–23149. [https:
1538 //proceedings.neurips.cc/paper_files/paper/2022/file/
1539 9278abf072b58caf21d48dd670b4c721-Paper-Conference.
1540 pdf](https://proceedings.neurips.cc/paper_files/paper/2022/file/9278abf072b58caf21d48dd670b4c721-Paper-Conference.pdf)
- 1541 Disberg, P., & Mandel, I. 2025, *ApJL*, 989, L8,
1542 doi: [10.3847/2041-8213/adf286](https://doi.org/10.3847/2041-8213/adf286)
- 1543 Doroshenko, V. 2024, arXiv e-prints, arXiv:2403.03127,
1544 doi: [10.48550/arXiv.2403.03127](https://doi.org/10.48550/arXiv.2403.03127)
- 1545 Duncan, R. C., & Thompson, C. 1992, *ApJL*, 392, L9,
1546 doi: [10.1086/186413](https://doi.org/10.1086/186413)

- 1547 Edwards, R. T., Bailes, M., Van Straten, W., & Britton,
1548 M. C. 2001, *Monthly Notices of the Royal Astronomical*
1549 *Society*, 326, 358
- 1550 Esposito, P., Rea, N., & Israel, G. L. 2021, in *Astrophysics*
1551 *and Space Science Library*, Vol. 461, *Astrophysics and*
1552 *Space Science Library*, ed. T. M. Belloni, M. Méndez, &
1553 C. Zhang, 97–142, doi: [10.1007/978-3-662-62110-3_3](https://doi.org/10.1007/978-3-662-62110-3_3)
- 1554 Faucher-Giguère, C.-A., & Kaspi, V. M. 2006, *ApJ*, 643,
1555 332, doi: [10.1086/501516](https://doi.org/10.1086/501516)
- 1556 Gardenier, D. W., & van Leeuwen, J. 2021, *A&A*, 651, A63,
1557 doi: [10.1051/0004-6361/202040119](https://doi.org/10.1051/0004-6361/202040119)
- 1558 Gavriil, F. P., Gonzalez, M. E., Gotthelf, E. V., et al. 2008,
1559 *Science*, 319, 1802, doi: [10.1126/science.1153465](https://doi.org/10.1126/science.1153465)
- 1560 Gehrels, N., Chincarini, G., Giommi, P., et al. 2004, *ApJ*,
1561 611, 1005, doi: [10.1086/422091](https://doi.org/10.1086/422091)
- 1562 Gençali, A. A., & Ertan, Ü. 2024, *MNRAS*, 534, 1481,
1563 doi: [10.1093/mnras/stae2177](https://doi.org/10.1093/mnras/stae2177)
- 1564 Glorot, X., & Bengio, Y. 2010, in *Proceedings of Machine*
1565 *Learning Research*, Vol. 9, *Proceedings of the Thirteenth*
1566 *International Conference on Artificial Intelligence and*
1567 *Statistics*, ed. Y. W. Teh & M. Titterton (Chia
1568 Laguna Resort, Sardinia, Italy: PMLR), 249–256.
1569 <https://proceedings.mlr.press/v9/glorot10a.html>
- 1570 Górski, K. M., Hivon, E., Banday, A. J., et al. 2005, *ApJ*,
1571 622, 759, doi: [10.1086/427976](https://doi.org/10.1086/427976)
- 1572 Graber, V., Ronchi, M., Pardo-Araujo, C., & Rea, N. 2024,
1573 *ApJ*, 968, 16, doi: [10.3847/1538-4357/ad3e78](https://doi.org/10.3847/1538-4357/ad3e78)
- 1574 Greenberg, D. S., Nonnenmacher, M., & Macke, J. H. 2019,
1575 arXiv e-prints, arXiv:1905.07488,
1576 doi: [10.48550/arXiv.1905.07488](https://doi.org/10.48550/arXiv.1905.07488)
- 1577 Gullón, M., Miralles, J. A., Viganò, D., & Pons, J. A. 2014,
1578 *MNRAS*, 443, 1891, doi: [10.1093/mnras/stu1253](https://doi.org/10.1093/mnras/stu1253)
- 1579 Gullón, M., Pons, J. A., Miralles, J. A., et al. 2015,
1580 *MNRAS*, 454, 615, doi: [10.1093/mnras/stv1644](https://doi.org/10.1093/mnras/stv1644)
- 1581 Harding, A. K. 2013, *Frontiers of Physics*, 8, 679,
1582 doi: [10.1007/s11467-013-0285-0](https://doi.org/10.1007/s11467-013-0285-0)
- 1583 Harris, C. R., Jarrod Millman, K., van der Walt, S. J., et al.
1584 2020, *Nature*, 585, 357, doi: [10.1038/s41586-020-2649-2](https://doi.org/10.1038/s41586-020-2649-2)
- 1585 He, K., Zhang, X., Ren, S., & Sun, J. 2015, preprint,
1586 arXiv:1502.01852
- 1587 Hermans, J., Delaunoy, A., Rozet, F., et al. 2021, arXiv
1588 e-prints, arXiv:2110.06581,
1589 doi: [10.48550/arXiv.2110.06581](https://doi.org/10.48550/arXiv.2110.06581)
- 1590 Hunter, J. D. 2007, *Comput. Sci. Eng.*, 9, 90,
1591 doi: [10.1109/MCSE.2007.55](https://doi.org/10.1109/MCSE.2007.55)
- 1592 Inserra, C., Smartt, S. J., Jerkstrand, A., et al. 2013, *ApJ*,
1593 770, 128, doi: [10.1088/0004-637X/770/2/128](https://doi.org/10.1088/0004-637X/770/2/128)
- 1594 Jacoby, B. A., Bailes, M., Ord, S. M., Edwards, R. T., &
1595 Kulkarni, S. R. 2009, *ApJ*, 699, 2009,
1596 doi: [10.1088/0004-637X/699/2/2009](https://doi.org/10.1088/0004-637X/699/2/2009)
- 1597 Johnston, S., Smith, D. A., Karastergiou, A., & Kramer, M.
1598 2020, *MNRAS*, 497, 1957, doi: [10.1093/mnras/staa2110](https://doi.org/10.1093/mnras/staa2110)
- 1599 Jones, E., Oliphant, T. E., Peterson, P., et al. 2001, *SciPy*:
1600 Open source scientific tools for Python.
1601 <http://www.scipy.org/>
- 1602 Kaspi, V. M., & Beloborodov, A. M. 2017, *ARA&A*, 55,
1603 261, doi: [10.1146/annurev-astro-081915-023329](https://doi.org/10.1146/annurev-astro-081915-023329)
- 1604 Keane, E., Bhattacharyya, B., Kramer, M., et al. 2015, in
1605 *Advancing Astrophysics with the Square Kilometre*
1606 *Array (AASKA14)*, 40, doi: [10.22323/1.215.0040](https://doi.org/10.22323/1.215.0040)
- 1607 Keane, E. F., & Kramer, M. 2008, *MNRAS*, 391, 2009,
1608 doi: [10.1111/j.1365-2966.2008.14045.x](https://doi.org/10.1111/j.1365-2966.2008.14045.x)
- 1609 Keane, E. F., Graber, V., Levin, L., et al. 2025, *The Open*
1610 *Journal of Astrophysics*, 8, 54256,
1611 doi: [10.33232/001c.154256](https://doi.org/10.33232/001c.154256)
- 1612 Keith, M. J., Jameson, A., van Straten, W., et al. 2010,
1613 *MNRAS*, 409, 619, doi: [10.1111/j.1365-2966.2010.17325.x](https://doi.org/10.1111/j.1365-2966.2010.17325.x)
- 1614 Kingma, D. P., & Ba, J. 2014, arXiv e-prints,
1615 arXiv:1412.6980, doi: [10.48550/arXiv.1412.6980](https://doi.org/10.48550/arXiv.1412.6980)
- 1616 Kurpas, J., Pires, A. M., Schwobe, A. D., et al. 2026, *A&A*,
1617 705, A148, doi: [10.1051/0004-6361/202556815](https://doi.org/10.1051/0004-6361/202556815)
- 1618 Lam, S. K., Pitrou, A., & Seibert, S. 2015, in *Proc. Second*
1619 *Workshop on the LLVM Compiler Infrastructure in HPC*,
1620 1–6, doi: [10.1145/2833157.2833162](https://doi.org/10.1145/2833157.2833162)
- 1621 Lander, S. K. 2023, *ApJL*, 947, L16,
1622 doi: [10.3847/2041-8213/acca1f](https://doi.org/10.3847/2041-8213/acca1f)
- 1623 Li, C., Zhao, G., Jia, Y., et al. 2019, *ApJ*, 871, 208,
1624 doi: [10.3847/1538-4357/aafa17](https://doi.org/10.3847/1538-4357/aafa17)
- 1625 Lorimer, D. R., & Kramer, M. 2012, *Handbook of Pulsar*
1626 *Astronomy* (Cambridge University Press)
- 1627 Lorimer, D. R., Faulkner, A. J., Lyne, A. G., et al. 2006,
1628 *MNRAS*, 372, 777, doi: [10.1111/j.1365-2966.2006.10887.x](https://doi.org/10.1111/j.1365-2966.2006.10887.x)
- 1629 Lü, H.-J., & Zhang, B. 2014, *ApJ*, 785, 74,
1630 doi: [10.1088/0004-637X/785/1/74](https://doi.org/10.1088/0004-637X/785/1/74)
- 1631 Lueckmann, J.-M., Goncalves, P. J., Bassetto, G., et al.
1632 2017, arXiv e-prints, arXiv:1711.01861,
1633 doi: [10.48550/arXiv.1711.01861](https://doi.org/10.48550/arXiv.1711.01861)
- 1634 Lyutikov, M., & Gavriil, F. P. 2006, *MNRAS*, 368, 690,
1635 doi: [10.1111/j.1365-2966.2006.10140.x](https://doi.org/10.1111/j.1365-2966.2006.10140.x)
- 1636 Makarenko, E. I., Igoshev, A. P., & Kholtygin, A. F. 2021,
1637 *MNRAS*, 504, 5813, doi: [10.1093/mnras/stab1175](https://doi.org/10.1093/mnras/stab1175)
- 1638 Manchester, R. N., Hobbs, G. B., Teoh, A., & Hobbs, M.
1639 2005, *AJ*, 129, 1993, doi: [10.1086/428488](https://doi.org/10.1086/428488)
- 1640 Manchester, R. N., Lyne, A. G., Camilo, F., et al. 2001,
1641 *MNRAS*, 328, 17, doi: [10.1046/j.1365-8711.2001.04751.x](https://doi.org/10.1046/j.1365-8711.2001.04751.x)
- 1642 Marino, A., Dehman, C., Kowlakas, K., et al. 2024, *Nature*
1643 *Astronomy*, 8, 1020, doi: [10.1038/s41550-024-02291-y](https://doi.org/10.1038/s41550-024-02291-y)

- 1644 McKinney, W. 2010, in Proceedings of the 9th Python in
1645 Science Conference, ed. S. van der Walt & J. Millman,
1646 51–56. [http://conference.scipy.org/proceedings/
1647 scipy2010/mckinney.html](http://conference.scipy.org/proceedings/scipy2010/mckinney.html)
- 1648 Metzger, B. D., Giannios, D., Thompson, T. A.,
1649 Bucciantini, N., & Quataert, E. 2011, MNRAS, 413,
1650 2031, doi: [10.1111/j.1365-2966.2011.18280.x](https://doi.org/10.1111/j.1365-2966.2011.18280.x)
- 1651 Mishra-Sharma, S., & Cranmer, K. 2022, PhRvD, 105,
1652 063017, doi: [10.1103/PhysRevD.105.063017](https://doi.org/10.1103/PhysRevD.105.063017)
- 1653 Morello, V., Barr, E. D., Stappers, B. W., Keane, E. F., &
1654 Lyne, A. G. 2020, MNRAS, 497, 4654,
1655 doi: [10.1093/mnras/staa2291](https://doi.org/10.1093/mnras/staa2291)
- 1656 Narayan, R., & Ostriker, J. P. 1990, ApJ, 352, 222,
1657 doi: [10.1086/168529](https://doi.org/10.1086/168529)
- 1658 Nobili, L., Turolla, R., & Zane, S. 2008, MNRAS, 386,
1659 1527, doi: [10.1111/j.1365-2966.2008.13125.x](https://doi.org/10.1111/j.1365-2966.2008.13125.x)
- 1660 Oliphant, T. E. 2006, A guide to NumPy (USA: Trelgol
1661 Publishing)
- 1662 Page, D., Lattimer, J. M., Prakash, M., & Steiner, A. W.
1663 2004, ApJS, 155, 623, doi: [10.1086/424844](https://doi.org/10.1086/424844)
- 1664 Papamakarios, G., & Murray, I. 2016, arXiv e-prints,
1665 arXiv:1605.06376, doi: [10.48550/arXiv.1605.06376](https://doi.org/10.48550/arXiv.1605.06376)
- 1666 Pardo-Araujo, C., Rea, N., Ronchi, M., & Graber, V. 2026,
1667 arXiv e-prints, arXiv:2601.16159,
1668 doi: [10.48550/arXiv.2601.16159](https://doi.org/10.48550/arXiv.2601.16159)
- 1669 Pardo-Araujo, C., Ronch, M., Graber, V., & Rea, N. 2025,
1670 A&A, 696, A114, doi: [10.1051/0004-6361/202453314](https://doi.org/10.1051/0004-6361/202453314)
- 1671 Pastor-Marazuela, I., van Leeuwen, J., Bilous, A., et al.
1672 2025, A&A, 693, A279,
1673 doi: [10.1051/0004-6361/202450953](https://doi.org/10.1051/0004-6361/202450953)
- 1674 Paszke, A., Gross, S., Massa, F., et al. 2019, preprint,
1675 arXiv:1912.01703. <https://arxiv.org/abs/1912.01703>
- 1676 Pearson, J. M., Chamel, N., Potekhin, A. Y., et al. 2018,
1677 MNRAS, 481, 2994, doi: [10.1093/mnras/sty2413](https://doi.org/10.1093/mnras/sty2413)
- 1678 Perez, F., & Granger, B. E. 2007, Comput. Sci. Eng., 9, 21,
1679 doi: [10.1109/MCSE.2007.53](https://doi.org/10.1109/MCSE.2007.53)
- 1680 Perna, R., & Pons, J. A. 2011, ApJL, 727, L51,
1681 doi: [10.1088/2041-8205/727/2/L51](https://doi.org/10.1088/2041-8205/727/2/L51)
- 1682 Pétri, J. 2019, MNRAS, 485, 4573,
1683 doi: [10.1093/mnras/stz711](https://doi.org/10.1093/mnras/stz711)
- 1684 Philippov, A., Tchekhovskoy, A., & Li, J. G. 2014,
1685 MNRAS, 441, 1879, doi: [10.1093/mnras/stu591](https://doi.org/10.1093/mnras/stu591)
- 1686 Pons, J. A., Viganò, D., & Rea, N. 2013, Nature Physics, 9,
1687 431, doi: [10.1038/nphys2640](https://doi.org/10.1038/nphys2640)
- 1688 Popov, S. B. 2023, Universe, 9, 273,
1689 doi: [10.3390/universe9060273](https://doi.org/10.3390/universe9060273)
- 1690 Popov, S. B., Pons, J. A., Miralles, J. A., Boldin, P. A., &
1691 Posselt, B. 2010, MNRAS, 401, 2675,
1692 doi: [10.1111/j.1365-2966.2009.15850.x](https://doi.org/10.1111/j.1365-2966.2009.15850.x)
- 1693 Posselt, B., Karastergiou, A., Johnston, S., et al. 2023,
1694 MNRAS, 520, 4582, doi: [10.1093/mnras/stac3383](https://doi.org/10.1093/mnras/stac3383)
- 1695 Potekhin, A. Y., Pons, J. A., & Page, D. 2015, SSRv, 191,
1696 239, doi: [10.1007/s11214-015-0180-9](https://doi.org/10.1007/s11214-015-0180-9)
- 1697 Qu, Y., & Bransgrove, A. 2026, ApJ, 998, 190,
1698 doi: [10.3847/1538-4357/ae3a9d](https://doi.org/10.3847/1538-4357/ae3a9d)
- 1699 Rea, N., Borghese, A., Esposito, P., et al. 2016, ApJL, 828,
1700 L13, doi: [10.3847/2041-8205/828/1/L13](https://doi.org/10.3847/2041-8205/828/1/L13)
- 1701 Rea, N., & De Grandis, D. 2025, arXiv e-prints,
1702 arXiv:2503.04442, doi: [10.48550/arXiv.2503.04442](https://doi.org/10.48550/arXiv.2503.04442)
- 1703 Rea, N., & Esposito, P. 2011, in Astrophysics and Space
1704 Science Proceedings, Vol. 21, High-Energy Emission from
1705 Pulsars and their Systems, ed. D. F. Torres & N. Rea,
1706 247, doi: [10.1007/978-3-642-17251-9_21](https://doi.org/10.1007/978-3-642-17251-9_21)
- 1707 Rea, N., Gullón, M., Pons, J. A., et al. 2015, ApJ, 813, 92,
1708 doi: [10.1088/0004-637X/813/2/92](https://doi.org/10.1088/0004-637X/813/2/92)
- 1709 Rea, N., Hurley-Walker, N., & Caleb, M. 2026, arXiv
1710 e-prints, arXiv:2601.10393,
1711 doi: [10.48550/arXiv.2601.10393](https://doi.org/10.48550/arXiv.2601.10393)
- 1712 Rea, N., Zane, S., Turolla, R., Lyutikov, M., & Götz, D.
1713 2008, ApJ, 686, 1245, doi: [10.1086/591264](https://doi.org/10.1086/591264)
- 1714 Ronchi, M., Graber, V., Garcia-Garcia, A., Rea, N., &
1715 Pons, J. A. 2021, ApJ, 916, 100,
1716 doi: [10.3847/1538-4357/ac05bd](https://doi.org/10.3847/1538-4357/ac05bd)
- 1717 Ronchi, M., Rea, N., Graber, V., & Hurley-Walker, N.
1718 2022, ApJ, 934, 184, doi: [10.3847/1538-4357/ac7cec](https://doi.org/10.3847/1538-4357/ac7cec)
- 1719 Rozwadowska, K., Vissani, F., & Cappellaro, E. 2021,
1720 NewA, 83, 101498, doi: [10.1016/j.newast.2020.101498](https://doi.org/10.1016/j.newast.2020.101498)
- 1721 Santangelo, A., Zane, S., Feng, H., et al. 2019, Science
1722 China Physics, Mechanics, and Astronomy, 62, 29505,
1723 doi: [10.1007/s11433-018-9234-3](https://doi.org/10.1007/s11433-018-9234-3)
- 1724 Sautron, M., McEwen, A. E., Younes, G., et al. 2025, ApJ,
1725 986, 88, doi: [10.3847/1538-4357/add0aa](https://doi.org/10.3847/1538-4357/add0aa)
- 1726 Sengar, R., Bailes, M., Balakrishnan, V., et al. 2025,
1727 MNRAS, 536, 3159, doi: [10.1093/mnras/stae2716](https://doi.org/10.1093/mnras/stae2716)
- 1728 Spitkovsky, A. 2006, ApJL, 648, L51, doi: [10.1086/507518](https://doi.org/10.1086/507518)
- 1729 Stratta, G., Dainotti, M. G., Dall’Osso, S., Hernandez, X.,
1730 & De Cesare, G. 2018, ApJ, 869, 155,
1731 doi: [10.3847/1538-4357/aadd8f](https://doi.org/10.3847/1538-4357/aadd8f)
- 1732 Tejero-Cantero, A., Boelts, J., Deistler, M., et al. 2020, The
1733 Journal of Open Source Software, 5, 2505,
1734 doi: [10.21105/joss.02505](https://doi.org/10.21105/joss.02505)
- 1735 Tong, H., Xu, R. X., Song, L. M., & Qiao, G. J. 2013, ApJ,
1736 768, 144, doi: [10.1088/0004-637X/768/2/144](https://doi.org/10.1088/0004-637X/768/2/144)
- 1737 Truemper, J. 1982, Advances in Space Research, 2, 241,
1738 doi: [10.1016/0273-1177\(82\)90070-9](https://doi.org/10.1016/0273-1177(82)90070-9)
- 1739 Turolla, R. 2009, in Astrophysics and Space Science Library,
1740 Vol. 357, Astrophysics and Space Science Library, ed.
1741 W. Becker, 141, doi: [10.1007/978-3-540-76965-1_7](https://doi.org/10.1007/978-3-540-76965-1_7)

- 1742 Turolla, R., Zane, S., & Watts, A. L. 2015, Reports on
1743 Progress in Physics, 78, 116901,
1744 doi: [10.1088/0034-4885/78/11/116901](https://doi.org/10.1088/0034-4885/78/11/116901)
- 1745 van der Walt, S., Colbert, S. C., & Varoquaux, G. 2011,
1746 Comput. Sci. Eng., 13, 22, doi: [10.1109/MCSE.2011.37](https://doi.org/10.1109/MCSE.2011.37)
- 1747 van Leeuwen, J., Kooistra, E., Oostrum, L., et al. 2023,
1748 A&A, 672, A117, doi: [10.1051/0004-6361/202244107](https://doi.org/10.1051/0004-6361/202244107)
- 1749 Vasist, M., Rozet, F., Absil, O., et al. 2023, A&A, 672,
1750 A147, doi: [10.1051/0004-6361/202245263](https://doi.org/10.1051/0004-6361/202245263)
- 1751 Verberne, S., & Vink, J. 2021, MNRAS, 504, 1536,
1752 doi: [10.1093/mnras/stab940](https://doi.org/10.1093/mnras/stab940)
- 1753 Viganò, D., Garcia-Garcia, A., Pons, J. A., Dehman, C., &
1754 Graber, V. 2021, Computer Physics Communications,
1755 265, 108001, doi: [10.1016/j.cpc.2021.108001](https://doi.org/10.1016/j.cpc.2021.108001)
- 1756 Viganò, D., & Pons, J. A. 2012, MNRAS, 425, 2487,
1757 doi: [10.1111/j.1365-2966.2012.21679.x](https://doi.org/10.1111/j.1365-2966.2012.21679.x)
- 1758 Viganò, D., Rea, N., Pons, J. A., et al. 2013, MNRAS, 434,
1759 123, doi: [10.1093/mnras/stt1008](https://doi.org/10.1093/mnras/stt1008)
- 1760 Virtanen, P., Gommers, R., Oliphant, T. E., et al. 2020,
1761 Nature Methods, 17, 261, doi: [10.1038/s41592-019-0686-2](https://doi.org/10.1038/s41592-019-0686-2)
- 1762 Voges, W., Aschenbach, B., Boller, T., et al. 1999, A&A,
1763 349, 389, doi: [10.48550/arXiv.astro-ph/9909315](https://doi.org/10.48550/arXiv.astro-ph/9909315)
- 1764 Wadiasingh, Z., & Timokhin, A. 2019, ApJ, 879, 4,
1765 doi: [10.3847/1538-4357/ab2240](https://doi.org/10.3847/1538-4357/ab2240)
- 1766 Wainscoat, R. J., Cohen, M., Volk, K., Walker, H. J., &
1767 Schwartz, D. E. 1992, ApJS, 83, 111, doi: [10.1086/191733](https://doi.org/10.1086/191733)
- 1768 Wang, Y., & van Leeuwen, J. 2024, A&A, 690, A377,
1769 doi: [10.1051/0004-6361/202450673](https://doi.org/10.1051/0004-6361/202450673)
- 1770 Watson, M. G., Auguères, J.-L., Ballet, J., et al. 2001,
1771 A&A, 365, L51, doi: [10.1051/0004-6361:20000067](https://doi.org/10.1051/0004-6361:20000067)
- 1772 Weisskopf, M. C., Brinkman, B., Canizares, C., et al. 2002,
1773 PASP, 114, 1, doi: [10.1086/338108](https://doi.org/10.1086/338108)
- 1774 Willingale, R., Starling, R. L. C., Beardmore, A. P., Tanvir,
1775 N. R., & O'Brien, P. T. 2013, MNRAS, 431, 394,
1776 doi: [10.1093/mnras/stt175](https://doi.org/10.1093/mnras/stt175)
- 1777 Wilms, J., Allen, A., & McCray, R. 2000, ApJ, 542, 914,
1778 doi: [10.1086/317016](https://doi.org/10.1086/317016)
- 1779 Xu, Y.-J., Peng, H.-L., Weng, S.-S., Zhang, X., & Ge, M.-Y.
1780 2025, ApJ, 981, 100, doi: [10.3847/1538-4357/adaebc](https://doi.org/10.3847/1538-4357/adaebc)
- 1781 Yamasaki, S., Lyubarsky, Y., Granot, J., & Göğüş, E. 2020,
1782 MNRAS, 498, 484, doi: [10.1093/mnras/staa2223](https://doi.org/10.1093/mnras/staa2223)
- 1783 Yao, J. M., Manchester, R. N., & Wang, N. 2017, ApJ, 835,
1784 29, doi: [10.3847/1538-4357/835/1/29](https://doi.org/10.3847/1538-4357/835/1/29)
- 1785 Zammit-Mangion, A., Sainsbury-Dale, M., & Huser, R.
1786 2025, Annual Review of Statistics and Its Application,
1787 12, 311, doi: [10.1146/annurev-statistics-112723-034123](https://doi.org/10.1146/annurev-statistics-112723-034123)
- 1788 Zane, S., Rea, N., Turolla, R., & Nobili, L. 2009, MNRAS,
1789 398, 1403, doi: [10.1111/j.1365-2966.2009.15190.x](https://doi.org/10.1111/j.1365-2966.2009.15190.x)
- 1790 Zhang, B., & Hu, R.-C. 2025, ApJL, 994, L20,
1791 doi: [10.3847/2041-8213/ae1023](https://doi.org/10.3847/2041-8213/ae1023)
- 1792 Zhang, L., Ridolfi, A., Li, D., et al. 2025, arXiv e-prints,
1793 arXiv:2512.17214, doi: [10.48550/arXiv.2512.17214](https://doi.org/10.48550/arXiv.2512.17214)
- 1794 Zhou, X., Huang, H.-T., Cheng, Q., & Zheng, X.-P. 2024,
1795 MNRAS, 530, 1636, doi: [10.1093/mnras/stae954](https://doi.org/10.1093/mnras/stae954)
- 1796 Zonca, A., Singer, L., Lenz, D., et al. 2019, The Journal of
1797 Open Source Software, 4, 1298, doi: [10.21105/joss.01298](https://doi.org/10.21105/joss.01298)